ADAPTIVE AND ROBUST TECHNIQUES (ART) FOR THERMOACOUSTIC TOMOGRAPHY

By

YAO XIE

A DISSERTATION PRESENTED TO THE GRADUATE SCHOOL
OF THE UNIVERSITY OF FLORIDA IN PARTIAL FULFILLMENT
OF THE REQUIREMENTS FOR THE DEGREE OF
MASTER OF SCIENCE

UNIVERSITY OF FLORIDA

2006

This thesis is dedicated to my parents.

ACKNOWLEDGMENTS

Foremost, I would like to thank my advisor, Professor Jian Li, for her support, encouragement, and guidance in the past two years. Dr. Li provided me the invaluable opportunity to investigate those fascinating research problems and always showed full confidence in me. She always encourages and directs me to develop immature ideas into a full-blown research paper; meanwhile, she sets a high standard for every work I have done. I wish I could live up to her expectation in my future career. Also, I am very grateful to my collaborator, Bin Guo, who has helped me a lot with his rich experience on breast cancer imaging and numerical simulations. I would like to thank Professor Petre Stoica, at Uppsala University, to teach me think critically and analyze problems rigorously. His comments and handwritten notes on signal processing problems have benefited me greatly. Professor Lihong Wang and Dr. Geng Ku at Texas A&M University, whose suggestions and experimental data have made this thesis more complete. I would thank all the lab members: Luzhou Xu, Xiayu Zheng, Xumin Zhu, William Roberts, Hong Xiong, Zhisong Wang, Yijun Sun, and Yanwei Wang, on myriads of help they have offered me during my two years in Spectral Analysis Lab. I would like to thank Professor Liuqing Yang and Professor Kenneth Slatton for serving in my dissertation committee. Thanks go to all my friends both at University of Florida and elsewhere who made the last two years full of enjoyment.

This dissertation is dedicated to my parents, for everything they did for me.

TABLE OF CONTENTS

LIST OF FIGURES

Abstract of Dissertation Presented to the Graduate School
of the University of Florida in Partial Fulfillment of the
Requirements for the Degree of Master of Science

ADAPTIVE AND ROBUST TECHNIQUES (ART)
FOR THERMOACOUSTIC TOMOGRAPHY

By

Yao Xie

August 2006

Chair: Jian Li
Major Department: Electrical and Computer Engineering

In this thesis, we present Adaptive and Robust Techniques (ART) for thermoacoustic tomography (TAT) for breast cancer detection. TAT is an emerging medical imaging technique that combines the merits of high contrast due to electromagnetic or laser stimulation and high resolution offered by thermal acoustic imaging. Image reconstruction via proper signal processing techniques is one of the key problems in TAT. The current image reconstruction methods used for TAT, such as the widely used Delay-and-Sum (DAS) approach, are data-independent and suffer from low resolution, high sidelobe levels, and poor interference rejection capabilities. Also, the amplitude and phase distortion problem of thermoacoustic signals due to propagation in the non-homogeneous media are not properly handled by the existing methods.

The data-adaptive ART can have much better resolution and much better interference rejection capabilities than their data-independent counterparts. By allowing certain uncertainties in the parameters, ART can be used to mitigate the amplitude and phase distortion problems encountered in TAT. Using both simulated and experimentally measured data, we demonstrate the excellent performance of ART: high resolution, low sidelobe level, and much better interference rejection capability.

CHAPTER 1
INTRODUCTION

1.1 Thermoacoustic Tomography

Thermoacoustic tomography (TAT) is a new technology with great promise in a wide span of biomedical applications (see, e.g., [1][3][4][5][6]). Its physical basis lies in the contrast of the radiation absorption rate among different biological tissues.

In TAT, a short electromagnetic pulse (e.g., microwave or laser) is used to illuminate the tissue. When the pulse is absorbed by the tissue, the heating results in expansion which generates acoustic signals. This phenomenon is called the thermoacoustic effect. The acoustic signals are recorded by wideband ultrasound transducer/transducers, which carry the information of tissue absorption properties. From the recorded thermoacoustic signals, an image of the tissue absorption properties is reconstructed. Such an image reveals the physiological and pathological status of the tissue, which has been used in many applications including breast cancer detection. The cancerous breast tissues have a two to five times higher microwave absorbtion rate than their surrounding normal breast tissues, which has been attributed to an increase in the amount of bound water and sodium within malignant cells [7][8][9].

TAT possesses both fine imaging resolution and good spatial contrast properties. Microwave imaging offers excellent contrast between cancerous and normal breast tissue, but the long wavelengths provide poor spatial resolution. Conventional ultrasound imaging has very fine spatial resolution but poor soft tissue contrast. Microwave-induced TAT takes advantage of both the high contrast of biological tissue in electromagnetic frequency band and the millimeter range spatial resolution due to the acoustic signals used in image reconstruction. In microwave-induced TAT, the

acoustic signal is usually below 2 MHz, resulting in the best axial resolution of 1 mm [10].

The key problem of TAT is how to map the microwave absorption property distribution from the measured signal, i.e., how to reconstruct the image. One method is to use the focused ultrasound transducers to localize the thermoacoustic sources in linear or sector scans and then obtain the images directly from the data, which is similar to the pulse-echo ultrasonography [11][12]. An alternative method is to use an array (real or synthetic aperture) of wideband point detectors to acquire thermoacoustic data and then reconstruct the absorption distribution. The later approach provides more flexibility to image reconstruction, which will be considered in this dissertation.

Although this dissertation only deals with tomography rather than 3-D imaging, the proposed ART methods could be easily extended to the 3-D imaging case as well. Herein tomography means that we form a cross sectional image of the tested tissue. In the tomography system, signals from the selected cross section of the tissue are recorded by focused transducers. One possible way to form a 3-D image of the tissue is to scan the cross section across different height. Another way is to use a three dimensional array of transducers to record signals from all heights and then reconstruct the 3-D image simultaneously.

1.2 Image Reconstruction Algorithms for TAT

1.2.1 Related Previous Work

Developing accurate and robust image reconstruction methods is one of the key challenges in TAT. Various image reconstruction algorithms have been developed for this purpose. By using Radon transformation on the TAT data function, reflectivity tomography reconstruction algorithms can be used for TAT image reconstruction [13]. Exact inverse solutions have been found for different scanning geometries in both the frequency domain [14][15] and the time domain [16][17]. Approximate reconstruction

algorithms, such as the time-domain Delay-and-Sum (DAS) beamforming method [18][19] and the optimal statistical approach [20], have also been proposed.

Time-domain approximate reconstruction algorithms such as the DAS type of data-independent approaches is widely used in medical imaging. In [19], un-weighted DAS is employed; in [18], the weights for DAS are chosen to be the transducer directivity to maximize the output Signal to Noise Ratio (SNR). The DAS type approaches need little prior information on the tissue for image reconstruction and can be fast and simple to implement to process the wideband acoustic signals. Although not based on the exact solution, they provide similar image qualities to those of the exact reconstruction algorithms.

However, these data-independent methods, including DAS, tend to suffer from poor resolution and high sidelobe level problems. Data-adaptive approaches, such as the recently introduced Robust Capon Beamforming (RCB) method [21][22], can have much better resolution and much better interference rejection capability than their data-independent counterparts.

1.2.2 Effects of Acoustic Heterogeneity

A common assumption of these existing methods is that the surrounding tissue is acoustically homogeneous. This approximation is inadequate in many medical imaging applications. According to previous studies, the sound speed in human female breast varies widely from 1430 m/s to 1570 m/s around the commonly assumed speed of 1510 m/s [23][24]. The heterogeneous acoustic properties of biological tissues cause amplitude and phase distortions in the recorded acoustic signals, which can result in significant degradations in image quality [25].

In Ultra-sound Tomography (UT), wavefront distortion due to heterogeneity of biological tissue has been studied extensively. Measurements of ultrasonic pulse amplitude and arrival time distortion have been obtained for abdominal wall [26] and human breast [27][28]. Various wavefront correction methods have been proposed

[29][30][31]. For example, in [26], a method based on the cross-correlation functions of the signals recorded by neighboring transducers is used to estimate the wavefront distortions and make corresponding correction. A more robust but complicated method, using cross correlation functions with respect to a reference waveform, which obtained from a group of recorded signals with high similarity, have also been proposed [31]. Various criterions for wavefront correction algorithms have been considered, including the mean-square error [30], and the speckle brightness [29]. A more recent approach was designed toward inverse filtering [32]. Some of the aforementioned methods could be borrowed for the purpose of phase distortion correction in thermoacoustic signals. However, they are not highly effective at correcting severe amplitude distortions [32][33], and they usually involve complicated procedures.

Also, the problem in TAT is somewhat different from that in UT. In the breast UT, the amplitude distortion caused by refraction is more problematic than the phase distortion induced by acoustic speed variation. In TAT, however, even for the biological tissue, such as the breast tissue, with a relatively weak heterogeneity, phase distortion dominates amplitude distortion [25]. This is due to the following reasons. First, thermoacoustic signals are mostly in a lower frequency range (usually below 1.5 MHz [10]) than those in UT. In the frequency range of TAT, ultrasound scattering is weak [24]. Second, in TAT, the acoustic signals are induced by electromagnetic absorption hence only have one-way propagation distortion due to transmission. In UT, either in the pulse-echo mode or in the transmission mode, two ways of distortions happen on the wave, during both the transmission and reception propagation. These unique features suggest that new adaptive and robust imaging techniques should be designed especially for TAT.

1.3 Contributions

In this thesis, we present new Adaptive and Robust Techniques (ART) based on RCB for TAT. ART can be used to mitigate the amplitude and phase distortion

problems in TAT by allowing certain uncertainties. Specifically, in the first step of ART, RCB is used for waveform estimation by treating the amplitude distortion with an uncertainty parameter. In the second step of ART, a simple yet effective peak searching method is used for phase distortion correction. Compared with other energy or amplitude based response intensity estimation methods, peak searching can be used to improve image quality with little additional computational costs. Moreover, since the acoustic pulse is usually bipolar: a positive peak, corresponding to the compression pulse, and a negative peak, corresponding to the rarefaction pulse [18], we can further enhance the image contrast in TAT by using the peak-to-peak difference as the response intensity for a focal point.

We will demonstrate the excellent performance of ART by using both data simulated on a 2-D breast model and data experimentally measured from mastectomy specimens and mouse brain. The numerical examples are designed to test the ability of ART to detect small tumor, to resolve closely located small tumors, and to form image of a large tumor with consistent size and shape. The experimental examples test the performance of ART in real biological tissues, and study the effects of choice of parameter in ART.

1.4 Dissertation Outline

In Chapter 2, we introduce the data model for a TAT imaging system. First, we preprocess the signals to compensate for the propagation loss, and time-shift to align all the signals from a focal point for further processing. The image reconstruction problem is formulated based on the preprocessed data. A brief review for the causes of the amplitude and phase distortions of the acoustic signals, and their effects on the reconstructed images is also given.

Chapter 3 presents the Adaptive and Robust Techniques (ART) for TAT. ART processes the wideband thermoacoustic signals in time domain. ART consists of three steps, waveform estimation, peak searching, and response intensity calculation. In the

first step, Robust Capon Beamforming (RCB) [21] is used for waveform estimation, and compared with the conventional Delay-and-Sum (DAS) approach. Step II of ART introduces peak searching which can effective mitigate the effect of phase distortion. In Step III, two types of response intensity calculation approaches, the energy based and amplitude based, are summarized and compared. We also present two new response intensity calculation methods based on the peak-searching results, which show advantages compared with the existing methods.

In Chapter 4, we presents some examples to study the performance of ART. The examples are based on both simulated and real-world experimental data. Compared with the data-independent and non-robust counterparts, ART has lower sidelobe level, higher resolution, and much better capability in rejecting interferences. Using the data from a simulated 2-D breast model, we show that ART can detect small tumor at accurate location, form an image of the large tumor with consistent shape and size, and resolve two closely located small tumors. Using the data experimentally obtained from a mastectomy breast specimen and mouse brain, we show that ART has meritorious performance in the real scenario. Also, the choice of parameters in ART are studied.

The conclusions and future work are given in Chapter 5.

CHAPTER 2
PRELIMINARY

2.1 Signal Model and Preprocessing

Consider a TAT imaging system as shown in Figure 2–1(a). A stimulating electromagnetic (laser or microwave) pulse is absorbed by the biological tissue under testing, which causes a sudden heat change (on the order of 10^{-4} degrees Celsius [34]). Due to the thermoacoustic effect, an acoustic pulse is generated which can be recorded by an ultrasonic transducer array. The transducer array may be a real aperture array or a synthetic aperture array formed by rotating a sensor around the tissue and record the acoustic waves at different locations. We assume that the number of transducers in the array (or in the synthetic aperture array case, the number of transducer data acquisition locations) is M. Each transducer is assumed to be omnidirectional; mutual couplings among the transducers are not considered in our model but the induced errors can be tolerated by our robust algorithms to a certain extent. The recorded acoustic signals are sufficiently sampled and digitized and a typical recorded pulse is shown in Figure 2–1(b) (base on the data measured on the breast specimen II described in Section 6). The data model for the sampled and digitized acoustic signal recorded by the mth transducer is given by:

$$x_m(n) = s_m(n) + \tilde{e}_m(n), \quad m = 1, \cdots, M. \tag{2–1}$$

where n is the discrete time index, starting from t_0 after excitation pulse. The scalar $s_m(n)$ denotes the signal component, which corresponds to the acoustic pulse generated at a focal point, and $\tilde{e}_m(n)$ is the residual term, which includes unmodelled noise and interference (caused by other sources within the tissue).

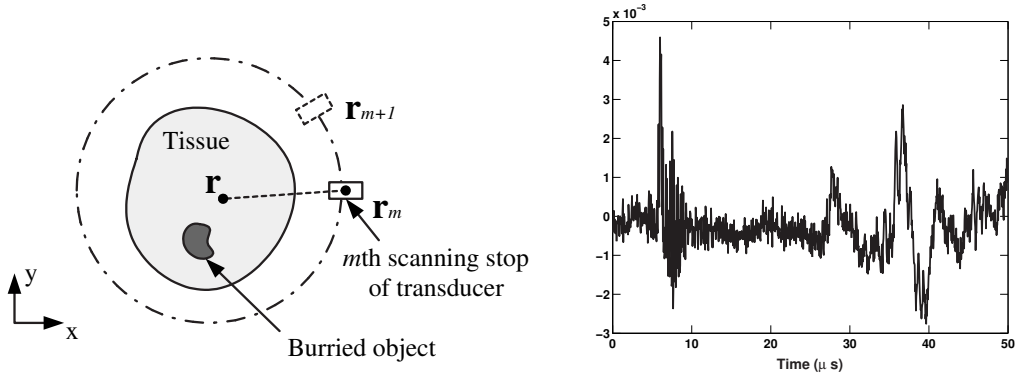

(a) (b)

Figure 2–1: (a): A schematic of a 2-D synthetic aperture based TAT scanning system; (b): a typical acoustic pulse recorded by a transducer (for data measured from breast specimen II).

The goal of ART is to reconstruct an image of thermoacoustic response intensity $I(\mathbf{r})$, which is directly related to the absorption property of the tissue, from the recorded data set $\{x_m(n)\}$. Herein the (2-D or 3-D) vector $\mathbf{r}$ denotes the focal point location coordinate. To form an image, we scan the focal point at location $\mathbf{r}$ to cover the entire cross-section of the tissue. We allow certain uncertainties in ART to deal with amplitude and phase distortions caused by the background heterogeneity.

The discrete arrival time of the pulse (for the mth transducer) can be determined approximately as:

$$t_m(\mathbf{r}) = \left\lfloor -\frac{t_0}{\Delta t} + \frac{\|\mathbf{r} - \mathbf{r}_m\|}{\Delta t v_0} \right\rfloor . \tag{2–2}$$

We will omit the dependence of the arrival time $t_m(\mathbf{r})$ on $\mathbf{r}$ hereafter for notational simplicity. Here Δt is the sampling interval, and the 3-D vector $\mathbf{r}_m$ denotes the location of the mth transducer. The sound speed v_0 is chosen to be the average sound speed of the biological tissue under interrogation. The notation $\|\mathbf{x}\|$ denotes the Euclidean norm of $\mathbf{x}$, and $\lfloor y \rfloor$ stands for rounding to the greatest integer less than y. The second term in (2–2) represents the time-of-flight between the focal point and the mth transducer.

The signal components $\{s_m(n)\}_{m=1}^M$ are approximately scaled and shifted versions of a nominal waveform $s(t)$ at the source:

$$s_m(n) \approx \frac{\exp\left(-\alpha\|\mathbf{r}-\mathbf{r}_m\|\right)}{\|\mathbf{r}-\mathbf{r}_m\|} \cdot s(n-t_m), \tag{2–3}$$

where α is the attenuation coefficient in Nepers/m. In TAT, the major frequency components of the acoustic signals take a relatively narrow band, and are usually lower than those in UT [25]. Hence we can approximate α as a frequency independent constant.

We preprocess the data to time delay all the signals from the focal point $\mathbf{r}$ and compensate for the loss in amplitude due to propagation decay. Let $y_m(n)$ denote the signal after preprocessing to backpropagate the detected signal to the source:

$$y_m(n) = \exp\left(\alpha\|\mathbf{r}-\mathbf{r}_m\|\right) \cdot \|\mathbf{r}-\mathbf{r}_m\| x_m(n+t_m); \tag{2–4}$$

then the received vector data model can be written as:

$$\mathbf{y}(n) = \mathbf{a}_0 s(n) + \mathbf{e}(n), \quad n = -N, \cdots, N, \tag{2–5}$$

where $\mathbf{a}_0$ is the corresponding steering vector, which is approximately equal to $\bar{\mathbf{a}} = [1, \cdots, 1]^T$, $\mathbf{y}(n) = [y_1(n), \cdots, y_M(n)]^T$, $\mathbf{e}(n)$ represents the noise and interference term after preprocessing, and $(\cdot)^T$ denotes the transpose. Here we define the time interval of interests for the signal $\mathbf{y}(t)$ to be from $-N$ to N, which means that we only take N samples before and after the approximate arrival time given in (2–2) for the focal point at $\mathbf{r}$. The value of N should be chosen large enough so that the interval from $-N$ to N covers the expected signal duration in the region of interest.

2.2 Waveform and Phase Distortions

In reality, both the amplitude and the phase (or pulse arrival time) of the acoustic pulse will be distorted. A major cause for these distortions is the acoustically heterogeneous background. Amplitude distortion is mainly due to the interferences caused

by multi-path, which is inevitable in the heterogeneous medium: refraction occurs due to acoustic speed mismatch across the tissue interface; consequently, acoustic pulses arrived at the transducer will be via different routes and interfere with each other.

On the other hand, phase distortion is mainly caused by the nonuniform sound speed. For example, in human female breast the sound speed can vary from 1430 m/s to 1570 m/s; therefore the actual arrival time will fluctuate around the approximately calculated time given in (2–2). Moreover, an inaccurate estimate of t_0 (t_0 is aligned with the focal point's signal arrival time) and the transducer calibration error may also contribute to the phase distortion.

One example for amplitude and phase distortion is shown in Figure 2–2. The signals are obtained from the second breast specimen in later experimental examples. The preprocessed signals recorded by three transducers are shown in Figure 2–2, where the dashed line corresponds the calculated arrival time of the peaks, and the arrows in each panel point to the actual peaks. Clearly the expected and the actual peak arrival time do not coincide; their differences are the phase distortion. The shape of the peaks are different, which is part of the amplitude distortion. Amplitude and phase distortion will blur the image, raise the image background noise level, lower the values of the object of interest, and consequently decrease the image contrast [25].

We mitigate the effects of these distortions by allowing $\mathbf{a}_0$ to belong to an uncertainty set centered at $\bar{\mathbf{a}}$ and by considering the signal arriving within the interval from $-N$ to N. Our ART algorithm consists of three steps: Step I, Robust Capon Beamforming (RCB) [21][22] for robust waveform estimation; Step II, peak-searching for phase aberration mitigation; Step III, intensity calculation for forming the final images.

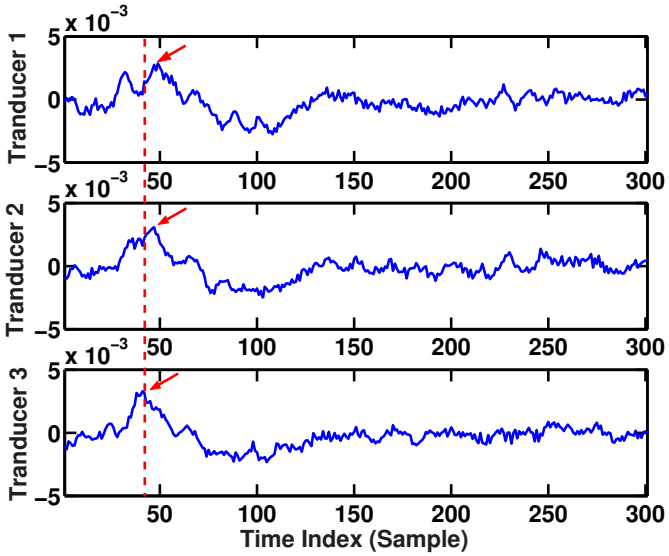

Figure 2–2: The preprocessed signal recorded by three transducers. The dashed red line corresponds to the calculated peak arrival time; the arrows in each panel point to the actual peaks.

CHAPTER 3
ADAPTIVE AND ROBUST TECHNIQUES (ART) FOR THERMOACOUSTIC TOMOGRAPHY

3.1 Step I of ART: Waveform Estimation

The first step of ART is to estimate the waveform of the acoustic pulse generated by the focal point at location $\mathbf{r}$, based on the data model in (2–5). Covariance fitting based RCB [35] is used to first estimate the steering vector $\mathbf{a}_0$, and use the estimated $\mathbf{a}_0$ to obtain an optimal beamformer weight vector for pulse waveform estimation.

It will appear that we have neglected the presence of phase distortion by using this data model in the first step. However, by allowing $\mathbf{a}_0$ to be uncertain, we can tolerate some phase distortions as well. This approximation causes little performance degradation to our robust algorithm.

3.1.1 Standard Capon Beamforming

The Capon beamformer [36] is a widely used data-adaptive beamforming method, which enjoys the advantages of better resolution, lower sidelobe level, and much better interference rejection capability than the data-independent methods. Capon beamformer selects the weight vector for waveform estimation adaptive according to the incoming data, to minimize the output power subject to the linear constraint that the signal-of-interest does not suffer from any distortion.

The common formulation of Capon is to determine a $M \times 1$ weight vector $\mathbf{w}$ to the following linearly constrained quadratic problem:

$$\min_{\mathbf{w}} \mathbf{w}^* \hat{\mathbf{R}} \mathbf{w} \quad \text{subject to} \quad \mathbf{w}^* \mathbf{a}_0 = 1, \tag{3–1}$$

where

$$\hat{\mathbf{R}} = \frac{1}{2N+1} \sum_{n=-N}^{N} \mathbf{y}(n)\mathbf{y}^T(n) \tag{3–2}$$

is the sample covariance matrix. Then the weight vector $\mathbf{w}$ is used to estimate signal waveform. The solution to (3–1) is easily derive:

$$\mathbf{w}_0 = \frac{\hat{\mathbf{R}}^{-1}\mathbf{a}_0}{\mathbf{a}_0^*\hat{\mathbf{R}}^{-1}\mathbf{a}_0}. \tag{3–3}$$

The Capon beamforming can also be reformulated into a covariance fitting form [35]:

$$\max_{\sigma^2} \sigma^2 \quad \text{subject to} \quad \hat{\mathbf{R}} - \sigma^2\mathbf{a}_0\mathbf{a}_0^* \geq 0. \tag{3–4}$$

The covariance fitting means that herein given $\hat{\mathbf{R}}$ and $\mathbf{a}_0$ we wish to determine the largest possible signal of interest term, $\sigma^2\mathbf{a}_0\mathbf{a}_0^*$, that can be a part of $\hat{\mathbf{R}}$ under the natural constraint that the noise covariance matrix is positive semi-definite.

The inherent problem of Capon is that, when the knowledge of the SOI steering vector is imprecise, it will suppress the signal-of-interest as a interference, which leads to a significant performance degradation. However, the steering vector mismatch is frequently encountered in practice, due to the looking angle direction errors, array calibration imperfection, source spreading and local scattering, as well as source wavefront distortions caused by the environment inhomogeneity [37].

3.1.2 Robust Capon Beamforming

Robust Capon Beamforming (RCB) [21][22][35] is one of most efficient methods proposed to solve the steering vector mismatch problem in Capon. By assuming that the true steering vector lies in the vicinity of the nominal steering vector $\bar{\mathbf{a}}$, RCB

consider the following optimization problem [21][22]:

$$\max_{\sigma^2,\mathbf{a}_0} \sigma^2 \quad \text{subject to} \quad \hat{\mathbf{R}} - \sigma^2 \mathbf{a}_0 \mathbf{a}_0^T \succeq 0, \quad \|\mathbf{a}_0 - \bar{\mathbf{a}}\|^2 \leq \varepsilon, \tag{3–5}$$

where $\mathbf{A} \succeq 0$ means that the matrix $\mathbf{A}$ is positive semi-definite, σ^2 is the power of the signal of interest. The second constraint in (3–5) is a spherical uncertainty set; an elliptical uncertainty set can be used instead if a tighter constraint is desirable [35].

The parameter ε in (3–5) determines the size of the uncertainty set and is a user parameter. To avoid the trivial solution of $\mathbf{a}_0 = 0$, we require that

$$\varepsilon < \|\bar{\mathbf{a}}\|^2. \tag{3–6}$$

It can be verified that the smaller the ε, the higher the resolution and the stronger the ability of RCB to suppress an interference that is close to the signal of interest, and that the larger the ε, the more robust RCB will be to tolerate distortions and small sample size problems caused by calculating $\hat{\mathbf{R}}$ in (3–2) from a finite number of data vectors or snapshots. When ε is close to M, RCB will perform like DAS. To attain high resolution and to effectively suppress interference, ε should be made as small as possible. On the other hand, the smaller the sample size N or the larger the distortions, the larger should ε be chosen [21][22]. Since the performance of RCB does not depend very critically on the choice of ε (as long as it is set to be a "reasonable value") [35], such qualitative guidelines are usually sufficient for making a choice of ε. We will investigate the effect of ε in Section 4. In our examples in Section 4, we choose certain reasonable initial values for ε, and then make some adjustments empirically based on image quality: making it smaller when the resulting images have low resolution, or making it larger when the image is distorted by interferences.

By using the Lagrange multiplier method, the solution to (3–5) is given by [21][22]:

$$\hat{\mathbf{a}}_0 = \bar{\mathbf{a}} - \left[\mathbf{I} + \mu\hat{\mathbf{R}}\right]^{-1} \bar{\mathbf{a}}, \tag{3–7}$$

where $\mathbf{I}$ is the identity matrix, $\mu \geq 0$ is the corresponding Lagrange multiplier that can be solved from the following equation:

$$\left\|(\mathbf{I} + \mu\hat{\mathbf{R}})^{-1}\bar{\mathbf{a}}\right\|^2 = \varepsilon. \tag{3–8}$$

Consider the eigendecomposition on the sample covariance matrix $\hat{\mathbf{R}}$:

$$\hat{\mathbf{R}} = \mathbf{U}\boldsymbol{\Gamma}\mathbf{U}^T, \tag{3–9}$$

where the columns of $\mathbf{U}$ are the eigenvectors of $\hat{\mathbf{R}}$ and the diagonal matrix $\boldsymbol{\Gamma}$ consists of the corresponding eigenvalues $\gamma_1 \geq \gamma_2 \geq \cdots \geq \gamma_M$. Let $\mathbf{b} = \mathbf{U}^T\bar{\mathbf{a}}$, where b_m denotes its mth element. Then (3–8) can be rewritten as

$$\mathcal{L}(\mu) = \sum_{m=1}^{M} \frac{|b_m|^2}{(1 + \mu\gamma_m)^2} = \varepsilon. \tag{3–10}$$

Note that $\mathcal{L}(\mu)$ is a monotonically decreasing function of μ, with $\mathcal{L}(0) > \varepsilon$ by $(3 - -6)$ and $\lim_{\mu\to\infty} \mathcal{L}(\mu) = 0 < \varepsilon$, which means that μ can be solved efficiently, say, by using the Newton's method (see [21] for more details). After obtaining the value of μ, the estimate $\hat{\mathbf{a}}_0$ of the actual steering vector $\mathbf{a}_0$ is determined by (3–7).

Observe that there is a "scaling ambiguity" in (3–5) by treating both the signal power σ^2 and the steering vector $\mathbf{a}_0$ as unknowns (see [21][35]). The ambiguity exists in the sense that $(\sigma^2, \mathbf{a}_0)$ and $(\sigma^2/c, c^{1/2}\mathbf{a}_0)$ (for any constant $c > 0$) yields the same term $\sigma^2\mathbf{a}_0\mathbf{a}_0^T$. To eliminate this ambiguity, we scale the solution $\hat{\mathbf{a}}_0$ to make its norm satisfy the following condition:

$$\|\hat{\mathbf{a}}_0\|^2 = M. \tag{3–11}$$

To obtain an estimate for the signal waveform $s(n)$, we apply a weight vector to the preprocessed signals $\{\mathbf{y}(n)\}_{n=-N}^{N}$. The weight vector is determined by using the estimated steering vector $\hat{\mathbf{a}}_0$ in the weight vector expression of the standard Capon beamformer (3–3):

$$\hat{\mathbf{w}}_{\text{RCB}} = \frac{\|\hat{\mathbf{a}}_0\|}{M^{1/2}} \cdot \frac{\left[\hat{\mathbf{R}} + \frac{1}{\mu}\mathbf{I}\right]^{-1} \bar{\mathbf{a}}_0}{\bar{\mathbf{a}}_0^T \left[\hat{\mathbf{R}} + \frac{1}{\mu}\mathbf{I}\right]^{-1} \hat{\mathbf{R}} \left[\hat{\mathbf{R}} + \frac{1}{\mu}\mathbf{I}\right]^{-1} \bar{\mathbf{a}}_0}. \tag{3–12}$$

Note that (3–12) has a diagonal loading form, which allows the sample covariance matrix to be rank-deficient. The beamformer output can be written as:

$$\hat{s}_{\text{RCB}}(n) = \hat{\mathbf{w}}_{\text{RCB}}^T \mathbf{y}(n), \quad n = -N, \cdots, N, \tag{3–13}$$

which is the waveform estimate for the acoustic pulse generated at the focal point at location $\mathbf{r}$.

3.1.3 Delay and Sum

RCB can provide a much better waveform estimate than the conventional DAS but at a higher computational cost. For a single focal point, RCB requires $O(M^3)$ flops, which mainly comes from the eigen-decomposition of the sample covariance matrix $\hat{\mathbf{R}}$ [21][22]; DAS needs only $O(M)$ flops. DAS can be used as a fast image reconstruction method to provide initial imaging results.

The weight vector used by (unweighed) DAS for waveform estimation is

$$\hat{\mathbf{w}}_{\text{DAS}} = \bar{\mathbf{a}}, \tag{3–14}$$

and the estimated waveform is given by

$$\hat{s}_{\text{DAS}}(n) = \hat{\mathbf{w}}_{\text{DAS}}^T \mathbf{y}(n) = \sum_{m=1}^{M} y_m(n), \quad n = -N, \cdots, N. \tag{3–15}$$

The weighted DAS [18] uses the transducer directivity rather than the uniform $1/M$ as the weights. Since the weights depend on transducer directivity and need to be measured in practice, we will not consider it herein.

3.2 Step II of ART: Peak Searching

Based on the estimated waveform obtained in Step I for the focal point at location $\mathbf{r}$, in Step II of ART, we will search for the two peaks of the bipolar acoustic pulse generated by the focal point. In a homogeneous background, where phase distortion is absent, we can accurately calculate the arrival time of the acoustic pulse generated by the focal point at location $\mathbf{r}$ by using (2–2). However, this is never true in heterogeneous biological tissues due to the nonuniform sound speed. It was reported in [25] that when the heterogeneity is weak, such as in the breast tissue, amplitude distortion caused by multi-path is not severe. We can assume that the original peak remains a peak in the waveform estimated from Step I of ART. Searching is performed within an interval around the calculated arrival time. The bipolar acoustic pulse has one peak positive and another negative. We determine the positive and negative peak values as follows:

$$P^{+} = \max\left\{\max_{n\in[-\Delta,\Delta]} \hat{s}(n), 0\right\}, \tag{3–16}$$

$$P^{-} = \min\left\{\min_{n\in[-\Delta,\Delta]} \hat{s}(n), 0\right\}, \tag{3–17}$$

where the searching range $[-\Delta, \Delta] \in [-N, N]$ is around the calculated arrival time given by (2–2). Here Δ is a user parameter. Since the peak searching is independent of the particular waveform estimation methods, we use $\hat{s}(n)$ to denote the waveform estimated by either DAS or ART.

The search range is determined by the difference between the true arrival time $\bar{t}_m$ and the calculated arrival time t_m based on (2–2). This arrival time difference has been analyzed for breast tissue by taking into account its relatively weak heterogeneity

acoustic property [25]. In [25], an expression for this difference is given by:

$$\delta_m(\mathbf{r}') = \bar{t}_m - t_m \propto \frac{[v(\mathbf{r}') - v_0]}{v_0}, \tag{3–18}$$

where $\mathbf{r}'$ is a point within the line connecting the focal point at location $\mathbf{r}$ and the mth transducer at location $\mathbf{r}_m$, and $v(\mathbf{r}')$ is the local sound speed. In (3–18), the higher order terms of $[v(\mathbf{r}') - v_0]/v_0$ have been ignored. It is reasonable to assume that $v(\mathbf{r}')$ is Gaussian distributed with mean v_0 and variance σ_v^2. Consequently the arrival time difference is also Gaussian distributed with zero-mean and variance $\sigma_\delta^2 \propto \sigma_v^2/v_0^2$. If we choose $\Delta = \sigma_\delta$, and the duration of the acoustic pulse is τ, we can find the two peaks of the pulse within the interval $(-\sigma_\delta, \sigma_\delta + \tau)$ on the recorded signals with a high probability of 0.6826. This analysis is consistent with the experimental measurements in [27][28]. From our examples, we found that a symmetric range $[-\Delta, \Delta]$ around the estimated arrival time performs similarly to the asymmetric range $[-\Delta, \Delta + \tau]$, and we use the former since it is easy to handle in practice. Also, we can use similar techniques as those in [27][28] to estimate σ_δ to find a good searching range for Step II of ART, and to estimate τ for the energy type methods, as shown in our examples later.

There is a tradeoff in choosing the searching range. The larger the searching range, the higher the probability we can find the peaks of the acoustic pulse within the range. However, if the range is chosen too large, the interferences may cause false peaks, and as a consequence, we are more likely to find a false peak. In our examples in Section 6, we choose the best searching range empirically based on the estimated variance of the arrival time difference $\hat{\sigma}_\delta$.

3.3 Step III of ART: Intensity Calculation

After estimating the waveform generated by the focal point at location $\mathbf{r}$, we need to obtain the response intensity based on the estimated waveform. For the same

estimated waveform, different approaches can be taken to evaluate the focal point response intensity. These approaches extract different information from the estimated waveform as the response intensity. The seemingly subtle differences among the intensity calculation methods can result in dramatic changes in the reconstructed image appearances. These different appearances may be useful to physicians in different ways.

There are two major types of response intensity measurement approaches: amplitude based and energy based. The waveform peak values obtained in Step II of ART can be used for both approaches.

Conventional DAS uses the amplitude based measure for TAT imaging [18][19][38], with the corresponding response intensity given by $\hat{s}(0)$, or equivalently:

$$I_{\mathrm{C}} = \hat{s}(0) = \sum_{m=1}^{M} y_m(0), \tag{3–19}$$

where the subscript "C" stands for "Conventional."

The energy based measure, such as the one used in [38], calculates the response intensity as follows:

$$I_{\mathrm{E1}} = \hat{s}^2(0) = \left[\sum_{m=1}^{M} y_m(0)\right]^2, \tag{3–20}$$

where the subscript "E1" means "Energy-type 1."

The entire pulse energy has also been used as an intensity measure, such as in the mono-static and multi-static microwave imaging for breast cancer detection [39][40][41], and the intensity is given by:

$$I_{\mathrm{E2}} = \sum_{n=0}^{\tau} \hat{s}^2(n) = \sum_{n=0}^{\tau} \left[\sum_{m=1}^{M} y_m(n)\right]^2, \tag{3–21}$$

where the subscript "E2" stands for "Energy-type 2."

We can consider using the peak value as the response intensity measure due to the bipolar nature of the response at the focal point:

$$I_{\text{P}} = \begin{cases} P^+ & \text{if } |P^+| \geq |P^-|; \\ P^- & \text{otherwise,} \end{cases} \tag{3–22}$$

where the subscript "P" stands for "Peak," with P^+ and P^- defined in (3–16) and (3–17), respectively. Herein we keep the sign of the maximum amplitude since the sign of the peak may also contain some information about the focal point.

Peak-searching maximizes the output signal-to-noise ratio. An intuitive explanation is that, given the fact that the acoustic pulse is bipolar [18], if we assume that the residual term $\mathbf{e}(t)$ is stationary, or its power is uniform over time, then the signal-to-noise ratio is maximized at the (positive or negative) peak of the acoustic pulse. As a comparison, the conventional DAS (3–19) fixes the samples to be summed up at the calculated arrival time. Due to phase distortions, the waveform at the calculated time may be far from the peak value.

We can also employ peak-to-peak difference as the response intensity for the focal point at location $\mathbf{r}$:

$$I_{\text{PP}} = P^+ - P^- \geq 0, \tag{3–23}$$

where the subscript "PP" denotes the "Peak-to-Peak difference." Peak-to-peak difference has higher imaging contrast than peak value measure: the peak-to-peak difference of the bipolar pulse is approximately twice the absolute peak value, which means that the output signal power of the former is four times of the latter; yet the noise power of the former is only twice of the latter. Therefore the output Signal-to-Noise Ratio (SNR) is doubled by using the peak-to-peak difference rather than the peak value.

Both peak-value and peak-to-peak difference measures belong to the amplitude based measures.

CHAPTER 4
NUMERICAL AND EXPERIMENTAL EXAMPLES

We demonstrate the performance of ART using both numerically simulated and experimentally measured 2-D TAT data. The ART images are compared with the DAS images.

4.1 Numerical Examples

4.1.1 Numerical Simulation Settings

We simulate a 2-D cylindrical breast model using the Finite-Difference Time-Domain (FDTD) [42] method. The 2-D breast model includes 2 mm thick skin, chest wall, as well as randomly distributed fatty breast tissues and glandular tissues. The cross-section of the breast model is a half circle with a 10 cm diameter. In the first numerical example, a 2 mm-diameter tumor is located at 2.2 cm below the skin (at $x = 7.0$ cm, $y = 6.0$ cm). Figure 4–2 shows the shape, dielectric properties and sound speed variations of the breast model, as well as tumor size and location for the first example. In the second numerical example, two 2 mm-diameter tumors are located at $x = 13.0$ cm, $y = 12.1$ cm, and at $x = 12.4$ cm, $y = 11.5$ cm, with only a 2-mm spacing between them. In our third example, one large tumor (1 cm in diameter) is located at $x = 12$ cm, $y = 15$ cm. Other properties of the breast model for the second and third examples are the same as those for the first example.

To reduce the reflections from the skin, the breast model is immersed in a lossless liquid with permittivity similar to that of the breast fatty tissue. Seventeen transducers are located on a half circle 10 mm away from the skin to form a real aperture array.

The dielectric properties of the breast tissues are assumed to be Gaussian random variables with variations of ±10% around their nominal values. This variation represents the upper bound reported in the literature. The nominal values are chosen to be typical of those reported in the literature [7][8][43][44][45], which is given in Table 1 [41]. The dielectric constants of glandular tissues are between $\epsilon_r = 11$ and $\epsilon_r = 15$. The dispersive properties of the fatty breast tissue and those of the tumor are also considered in the model. The randomly distributed fat breast tissues and glandular tissues with variable dielectric properties are representative of the non-homogeneity of the breast of an actual patient.

Following the report that the breast tissues have a weak acoustic heterogeneity [25], we model the sound speed within the breast as a Gaussian random variable with variation ±5% around the assumed average sound speed of 1500 m/s. Since the attenuation coefficient α in (2–3) is small for breast tissue (0.75 dB/MHz/cm) [24] and the acoustic signals are below 2 MHz, we neglect the exponential attenuation in acoustic wave propagation. Also, since the acoustic pressure field generated by the thermoacoustic effect is usually small [34], we do not consider the non-linear acoustic effects. The differential equations in [16] are used to characterize the thermoacoustic effect in our FDTD simulations. The probing microwave pulse used here is a modulated rectangular pulse with a modulating frequency of 800 MHz. The duration of the pulse is 1 μs.

In the following all the images are displayed on a linear scale, and we will name the imaging methods by their waveform estimation method followed by the intensity calculation approach, such as "DAS-C."

4.1.2 Preprocessing and Parameter Choice

Before applying the aforementioned preprocessing steps and ART, we remove the strong skin response using techniques similar to those in [38][41]. A calibration signal is obtained as the average of the recorded signals containing similar skin response.

Then the calibration signal is subtracted out from all recorded signals to remove the skin response as much as possible.

The searching range is chosen by the guidelines presented in Section 4. To obtain a general profile of the arrival time difference caused by the phase distortion, we use a simple method similar to the one used in [26]. First, the cross-correlation functions for all the signals recorded by the two neighboring transducers are obtained. The peak value of the cross-correlation function is used to estimate the arrival time delay between the signals recorded by the neighboring transducers. Second, these arrival time delays are fitted using a fourth-order polynomial curve, which is dominated by the arrival time delays due to the path length differences in the absent of phase distortions. The fourth-order polynomial is used since the delay caused by path length difference should vary smoothly [26]. Figure 4–3(a) shows the estimated arrival time delay and the delay based on curve fitting. Third, the delay difference between the estimated arrival time delay and the fitted delay, or the fitting error, is treated as the arrival time distortion for the transducers. The standard deviation of the delay difference is used to estimate σ_δ. Although the accuracy of the cross-correlation method is limited due to false peaks and jitter problems, it is sufficient to obtain a qualitative profile for σ_δ.

Figure 4–3 gives the histogram of the delay difference for all the cases we considered herein. For our simulated example, the standard deviation of the delay difference is 4.5, which indicates a weak phase distortion in the breast model. We set an initial value for Δ based on the estimated $\hat{\sigma}_\delta$, and adjust the length of the searching range to achieve the best imaging result.

To estimate the pulse duration $\hat{\tau}$ (used in DAS-E2 and RCB-E2), we select several typical signals (with clear peaks) and take the average of their pulse durations. In practice, the acoustic pulse duration is determined by the probing pulse duration, size and shape of the tumor, as well as the transducer response.

4.1.3 Examples

4.1.3.1 One Small Tumor

Figure 4–4 shows the images for the simulated breast model with one 2 mm - diameter tumor formed using ART and DAS. The tumor response is weak for such a small tumor. In these images we use $\varepsilon = 0.1M$ and the searching range [-14, 14]. Figure 4–4(a) corresponds to DAS-C, where the tumor is buried by interference and noise. In Figure 4–4(b), DAS-E1 fails to detect the tumor. In Figure 4–4(c), for DAS-E2, a shadow of the tumor can be seen. In Figure 4–4(d), for RCB-E2, most of the clutters are cleared up but a strong clutter shows up near the chest wall. Figures 4–4(e) - 4–4(h) show the results of peak searching; none of them have false tumors, which may be attributed to proper corrections of phase aberrations. Images produced by ART-P in Figure 4–4(f) and by ART-PP in Figure 4–4(h) have lower sidelobe levels and higher resolutions, and the latter has a higher contrast than the former, due to the latter using the peak-to-peak difference as the intensity measure.

4.1.3.2 Two Closely Located Small Tumors

This example demonstrates the fine resolution of ART. Figure 4–5 shows the images for the simulated breast model with two 2 mm - diameter tumors, spaced 2 mm away from each other. For this example we use $\varepsilon = 0.1M$ and searching range [-3, 3]. For this case, none of the DAS methods can resolve these two closely located tumors. Here we just show one DAS image, the DAS-PP image, in Figure 4–5(a). RCB-E2, in Figure 4–5(b), cannot resolve the tumors either. Both APT-P and APT-PP can resolve the two tumors, as shown in Figures 4–5(c) and 4–5(d), respectively. Close examinations of the images for RCB-E2 and ART-PP, shown in Figures 4–5(e) and 4–5(f), demonstrate the high resolution of ART.

4.1.3.3 One Large Tumor

Figure 4–6 shows the imaging results for the one large tumor (1 cm diameter) case. Here we set $\varepsilon = 0.1M$ and the searching range [-20, 20]. (Note that different

tumor sizes and locations will result in different sound speed variations in the breast model.) For the points inside the tumor sphere, The white circle in the image corresponds to the actual contour of the tumor. Although all the methods can detect the tumor, only ART can be used to form an image of the tumor with the best agreement with the actual tumor size and location.

Here the large tumor cannot be assumed a point source, but a 2-D circle. For a circle of radius r_s, zero-crossing points is offset from time 0 by $r_s/(v_0\Delta_t)$. We can make the searching range wider to take into this offset into account. In this 1 cm tumor case, the offset can be calculated to be about 10 samples. Note that the searching range width in our example (empirically decided for a good image quality) is 40, whereas in the previous 2 mm-diameter tumor case, the searching range width is 28 (empirically decided for a good image quality). We have increased the searching range width by 12 samples, which is consistent with our prediction.

Figure 4–7 shows a map of the values of μ used in ART, for each focal point. Due to the large range of μ, the maps are plotted on dB scale. Note that at the tumor locations, μ usually takes smaller value than other locations.

We measure the tumor location accuracy by the maximum pixel value in the image. Also, we define the Signal to Background Ratio (SBR) (i.e., squaring the pixel value of the image, the ratio of the maxima to total sum of squared value) as a image quality metric. Such measurements for the images formed by ART are summarized in Table 2. Note that in all cases ART can detect tumors at their true locations.

4.2 Experimental Results

We have also tested ART and DAS on three sets of TAT experimental data: two from mastectomy specimens [1], and another from the mouse brain, obtained by the Optical Imaging Laboratory at the Texas A&M University.

4.2.1 Experimental Settings

The fist two data sets were acquired from mastectomy specimens using a TAT system as shown in Figure 4–1. Microwave sources were used to heat the specimens transiently. In the experiment, the breast specimen was formed to a cylindrical shape inside a plastic bowl. The bowl was immersed in ultrasound coupling medium in a container. For breast specimen I, the acoustic signals were recorded at 240 equally spaced scanning stops on a circular track of radius 12.9 cm. The thickness of this specimen was about 4 cm in a round plastic bowl of 17 cm in diameter. This lesion was diagnosed as an invasive metaplastic carcinoma with chondroid and squamous metaplasia. The size of the tumor was measured to be 35 mm in diameter by TAT, and 36 mm in diameter by radiography (see [1] for details). For breast specimen II, the scanning radius was 9.7 cm, with 160 scanning stops. This specimen was 9 cm thick in a round plastic bowl of 11 cm in diameter. The lesion in the specimen was diagnosed as infiltrating lobular carcinoma; the size of the tumor was about 20 mm x 12 mm on TAT image, and about 26 mm x 15 mm on the radiography (see [1] for more details).

The third set of experimental data was obtained from a mouse brain. The data acquisition procedures are similar to those in [2]. The scanning radius was 3.15 cm, with 122 scanning stops. But unlike in [2], herein a microwave source was used to illuminate the mouse brain to obtain a absorption profile different to that in [2].

4.2.2 Parameter Choice

First, we study the delay difference profile for all the breast specimen and mouse brain data to get a qualitative guide for choosing the searching range in Step II of ART. The results are shown in Figures 4–3(c) to 4–3(e). Note that breast specimen II has a larger variance in delay differences than breast specimen I. In Figure 4–3(c), 70% of the delay differences are roughly between -23 to 23 samples, whereas in 4–3(c), 70% of the delay differences are between -40 and 40 samples. Therefore we should set

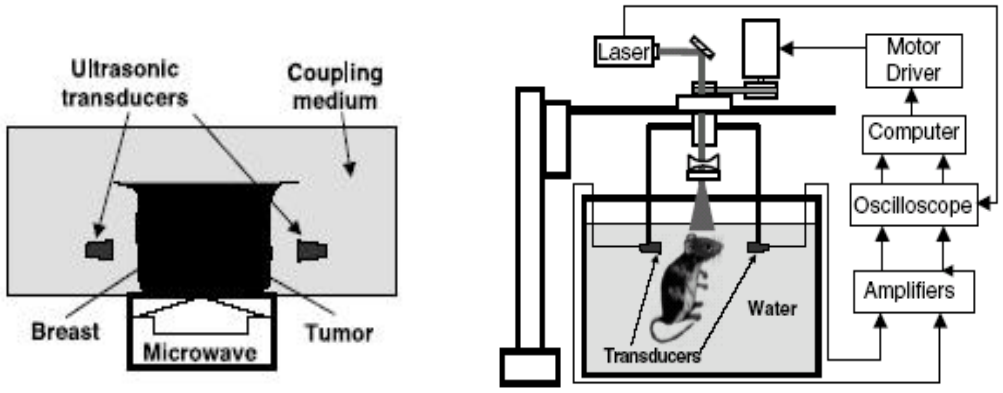

(a) (b)

Figure 4–1: The setting of the experimental TAT imaging system: (a): for breast specimens [1]; (b): for mouse brain [2].

a larger searching range for breast specimen II than for breast specimen I. In Figure 4–3(d), 70% of the delay difference are between -5 and 5 samples.

4.2.3 Examples

4.2.3.1 Breast Specimen I

Figure 4–8 shows the reconstructed images for breast specimen I. In the following images, the searching range was set to [-3, 3] after adjustment, and $\varepsilon = 0.5M$ for all the RCB used herein. In Figure 4–8(a), for DAS-C, the dark region shows an blurred object corresponding to the breast tumor. In Figure 4–8(b), for DAS-E1, the light region shows a vague boundary of the tumor. Figures 4–8(c), for DAS-E2, and 4–8(d), for RCB-E2, have similar performances. In Figures 4–8(e), for DAS-P, and 4–8(f), for ART-P, a dark region with a clear cut has a good correspondence with the location and shape of the tumor in the radiograph [1]. In Figures 4–8(g), for DAS-PP, and 4–8(h), for ART-PP, not only a clear image of the tumor is obtained, but also the detailed boundary is revealed. For comparison, the images from X-ray mammography and the exact inverse solution of TAT (see [1] for more details) are shown in Figures 4–8(i) and 4–8(j), respectively. We give Figure 4–8 and the following Figure 4–9 in grey scale to have a better comparison with the X-ray images.

4.2.3.2 Breast Specimen II

Figure 4–9 shows the reconstructed images for breast specimen II. The tumor size here is smaller, and a high level of interference and noise is present in the recorded data. The searching interval is eventually adjust to [-120, 120] and RCB parameter $\varepsilon = 0.5M$. In Figure 4–9(a), for DAS-C, the true tumor is barely identifiable from the surrounding clutters. The DAS-E1 shown in Figure 4–9(b) and the DAS-E2 shown in Figure 4–9(c) provide higher imaging contrast than DAS-C but show strong clutter. In Figure 4–9(d), for RCB-E2, a false tumor shows up, which demonstrates the need for robustness in the presence of relatively strong phase distortion. DAS-P is shown in Figure 4–9(e) and ART-P is shown in Figure 4–9(f). DAS-PP and ART-PP produce the best images in Figures 4–9(g) and 4–9(h), respectively, with the location and shape of the tumor consistent with the radiograph in Figure 4–9(i) [1]. If we define the Signal-to-Background Ratio (SBR) (i.e., squaring the pixel values of the image, the ratio of the maximum to the total sum of the squared values) as a image quality measurement metric, ART-PP has an SBR twice that of DAS-PP, which means a 3-dB gain for ART-PP. For comparison, the image formed by the exact inverse solution of TAT (see [1] for more details) is shown in Figure 4–9(j).

4.2.3.3 Mouse Brain

The imaging results for the mouse brain are shown in Figure 4–10. In the following images, the searching range was set to [-6, 6] after adjustment, and $\varepsilon = 0.6M$ for all the RCB used herein. Although the interpretations of the images need further consideration (for example, with the aid of image registration), we can observe the improvements of the image quality by using ART-PP. In Figure 4–10(f), ART-P shows more details, and the image is more clear than that of DAS-P, in Figure 4–10 (e). The energy based energy calculation methods, such as DAS-E2, in 4–10(c), and RCB-E2, in 4–10(d), tend to blur the details of the image. The images formed by

ART-P and ART-PP have the most details and interesting structures. The correspondence of their images with that formed by the exact inverse solution, in Figure 4–10(i), needs further study (see the future work section).

4.2.3.4 Effects of Parameters in ART

The effects of the uncertainty parameter ε in ART is studied in our next example. We vary ε of RCB used in ART. The imaging results for breast specimen I shown in Figure 4–11 are consistent with our previous analysis: when ε is large, the performance of RCB, in Figure 4–11(a), is close to that of DAS in Figure 4–8(g). When the parameter ε is small, as shown in Figure 4–11(c), the resolution is improved at the cost of robustness.

In our last example, the effect of the searching-range width on the imaging quality is considered. We use DAS-PP as an example since it shows more dependence on the searching range. The conclusion drawn for DAS applies to ART. A symmetric searching range centered around the calculated arrival time is used. From the discussions in Section 4, we know that there is a tradeoff in choosing the searching range. Clearly, when the searching range is too small, such as in Figure 4–12(a), we miss the true peaks. With an increase in the searching range, the image quality becomes gradually better as shown in Figures 4–12(b) and 4–12(c). However, when the searching range passes a certain threshold, with too much interference coming into the searching range, the image quality degrades because of increased clutters, as shown in Figure 4–12(d).

From our numerical and experimental examples, we conclude that ART has higher resolution and better interference rejection capability and more robustness against wavefront distortion than DAS. Also, we find that the amplitude-based measures reveal more details of the tumor in the reconstructed images than their energy-based counterparts. The energy-based measures are not sensitive to phase distortions;

however, they tend to blur the reconstructed images, causing lost of details with a low-pass filter like effect.

Table 4–1: Nominal Dielectric Properties of Breast Tissues [41].

Tissues	Dielectric Properties	
	Permittivity (F/m)	Conductivity (S/m)
Immersion Liquid	9	0
Chest Wall	50	7
Skin	36	4
Fatty Breast Tissue	9	0.4
Nipple	45	5
Glandular Tissue	11-15	0.4-0.5
Tumor	50	4

Table 4–2: Various Measurements of Images Formed by ART

Cases		Tumor Location (cm × cm)	SBR (dB)
One 2 mm Tumor Case	True location	(7.0, 6.0)	-
	ART-P	(6.9, 6.0)	-61.0
	ART-PP	(6.9, 6.0)	-59.3
Two 2 mm Tumors Case	True location	(7.0, 6.0) and (9.1, 6.9)	-
	ART-P	(6.9, 6.0) and (9.1, 6.9)	-60.0 and -60.8
	ART-PP	(6.9, 6.0) and (9.1, 6.9)	-59.9 and -61.0

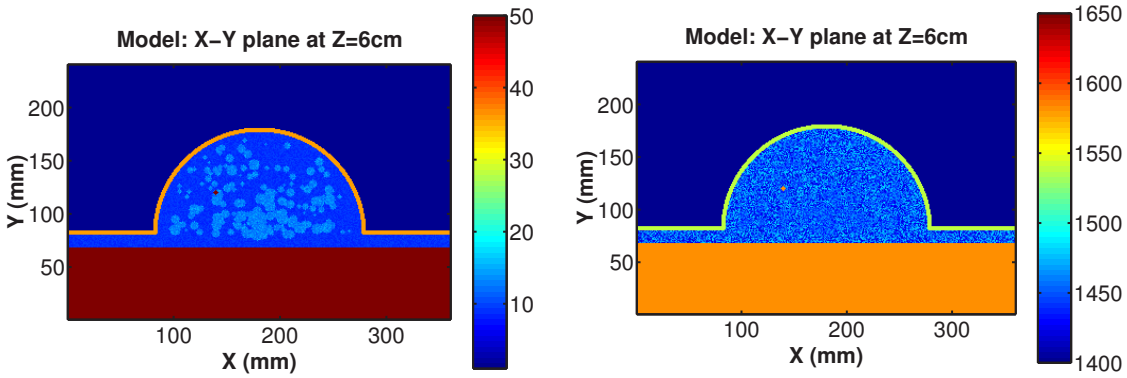

(a) (b)

Figure 4–2: The 2-D breast model in a x-y coordinate system, with a 2 mm - diameter tumor present. Different colors correspond to: (a): different permittivity values; (b): different sound speeds.

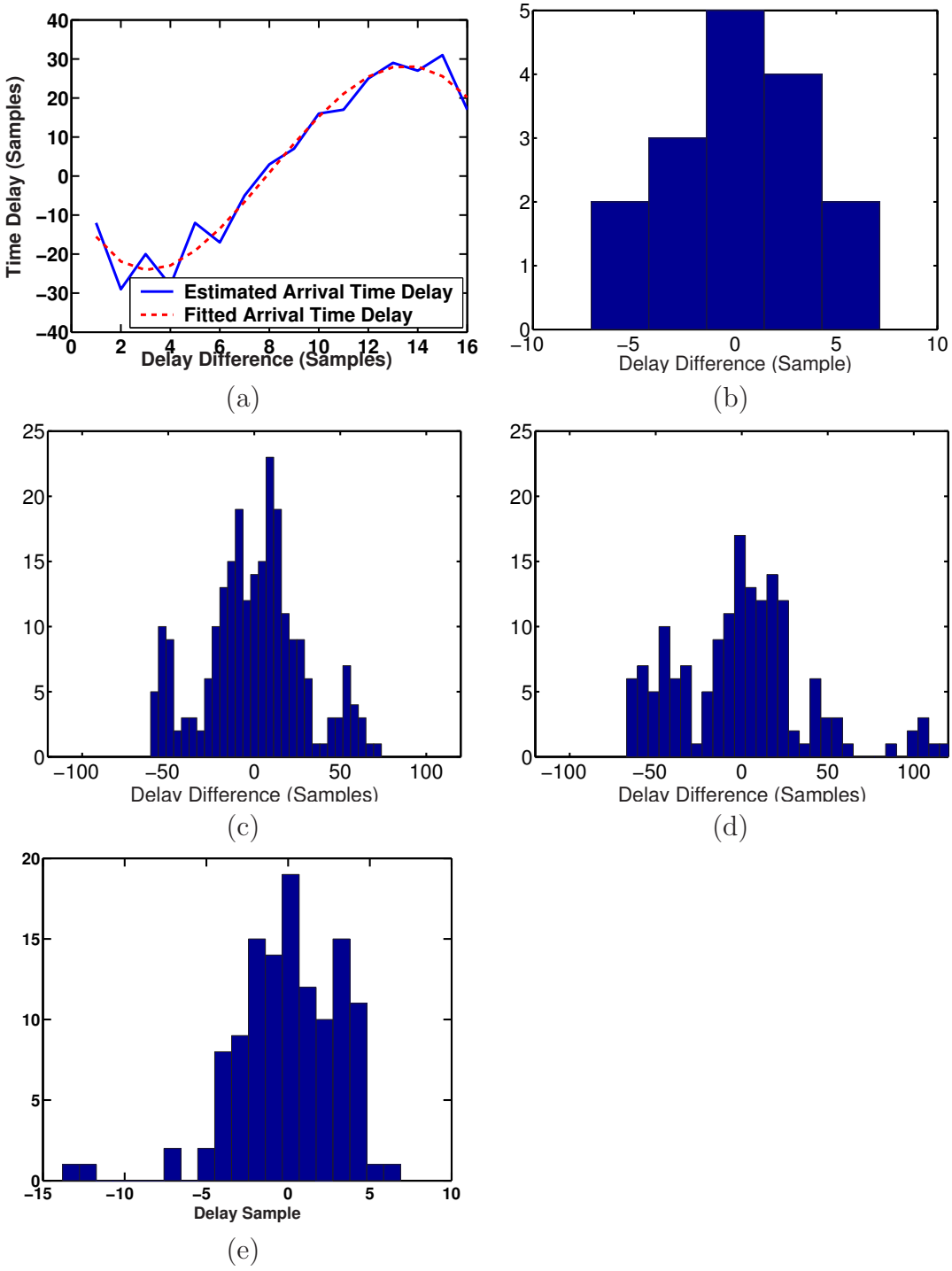

Figure 4–3: (a): Comparison between the estimated and fitted arrival time delays, for the simulated breast model with one tumor (the curves for two-tumor case are similar). Histograms of delay differences: (b): simulated breast model with one tumor; (c): breast specimen I; (d): breast specimen II; (e): mouse brain.

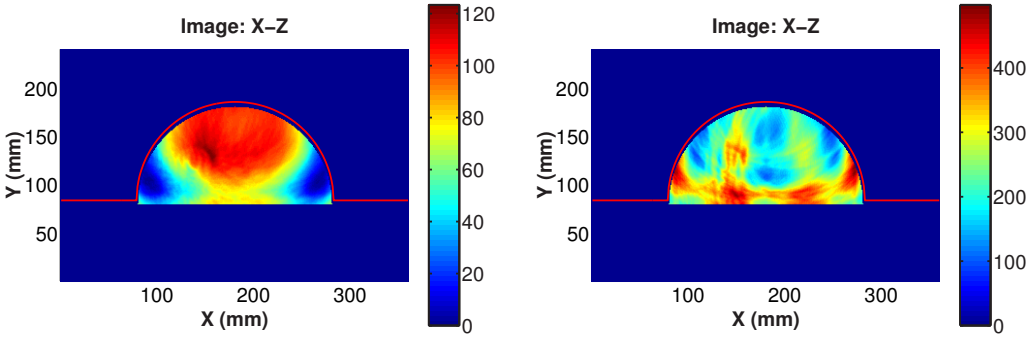

(a): DAS-C

(b): DAS-E1

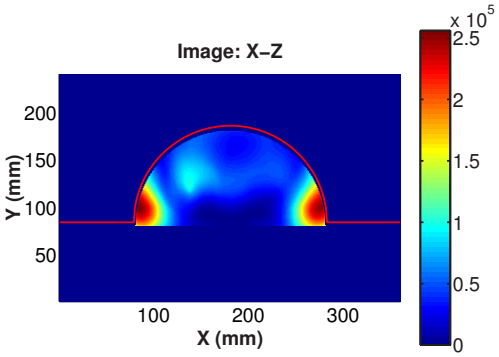

(c): DAS-E2

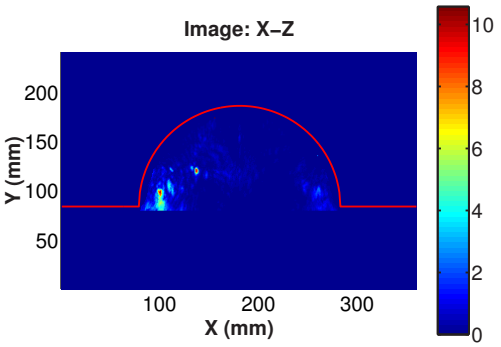

(d): RCB-E2

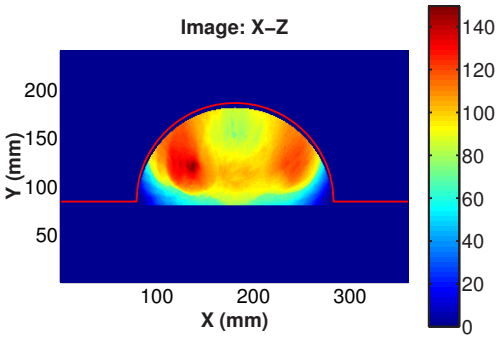

(e): DAS-P

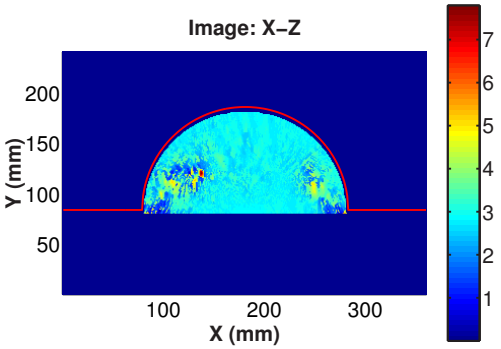

(f): ART-P

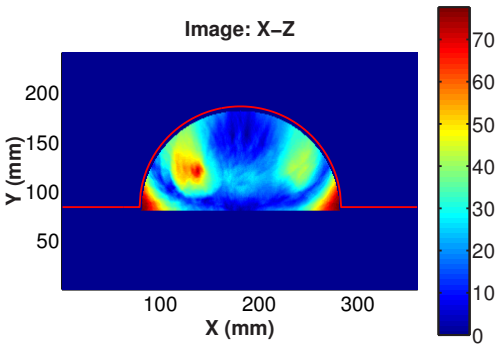

(g): DAS-PP

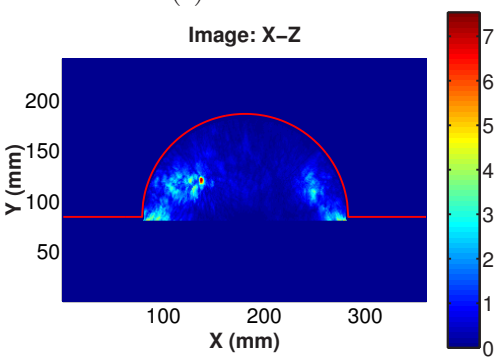

(h): ART-PP

Figure 4–4: Reconstructed images based on the 2-D simulated breast model with one 2 mm-diameter tumor. (a): DAS-C; (b): DAS-E1; (c) DAS-E2; (d): RCB-E2, with $\varepsilon = 0.1M$; (e): DAS-P; (f): ART-P, with $\varepsilon = 0.1M$; (g): DAS-PP; (h): ART-PP, with $\varepsilon = 0.1M$.

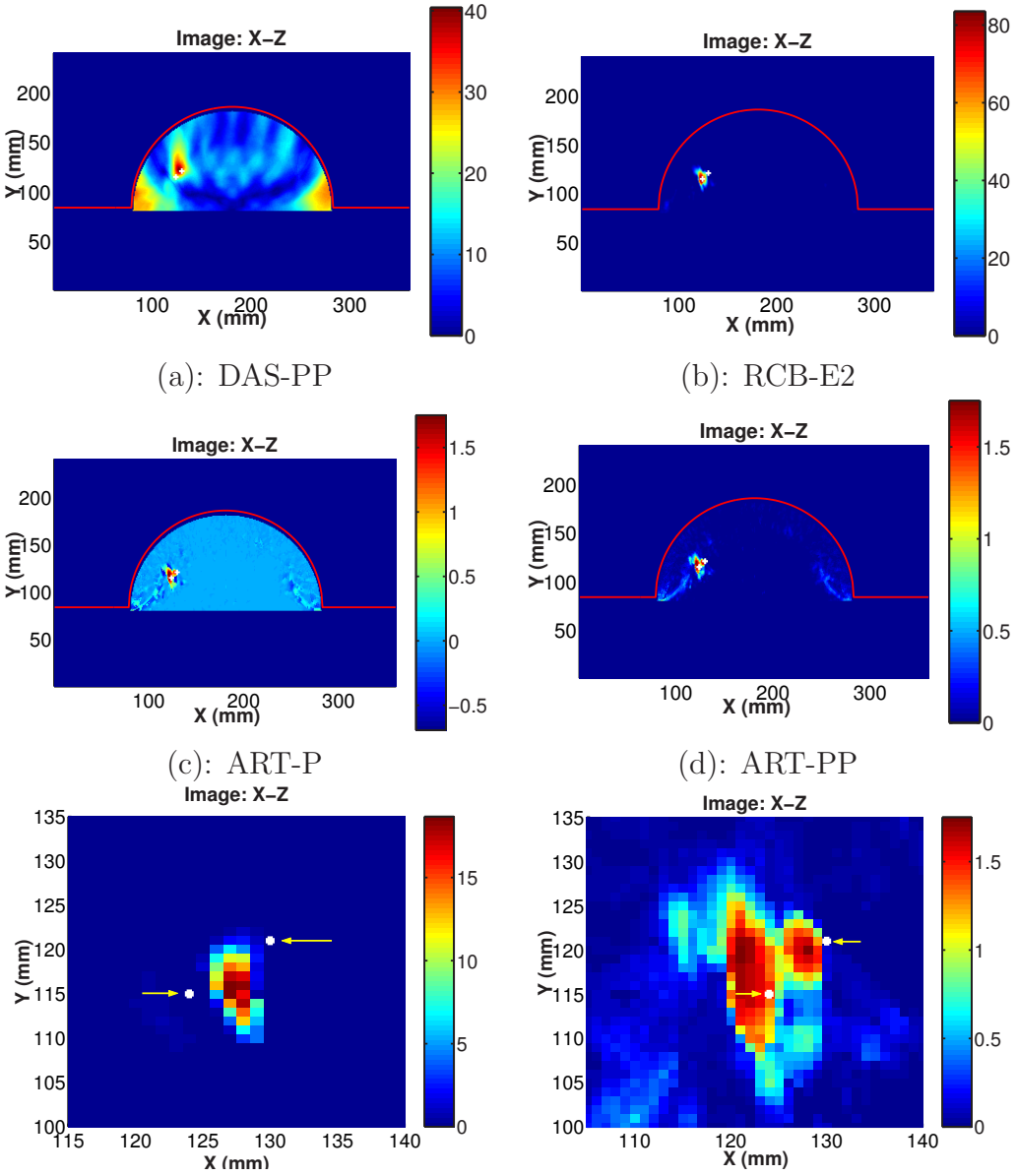

(a): DAS-PP (b): RCB-E2

(c): ART-P (d): ART-PP

(e): Zoom in of (b) (f): Zoom in of (d)

Figure 4–5: Reconstructed images based on the 2-D simulated breast model, with two closely located (2mm spacing) small tumors (2 mm in diameter). The parameter used in RCB and ART is $\varepsilon = 0.1M$. The white dots in (e) and (f) correspond to the actual (center) location of the tumors. (a): DAS-PP; (b): RCB-E2; (c) ART-P; (d): ART-PP, (e): zoom in of RCB-E2; (f): zoom in of ART-PP.

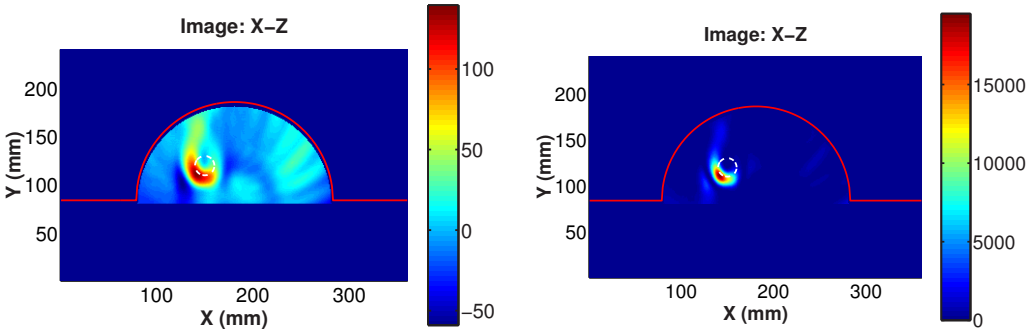

(a): DAS-C

(b): DAS-E1

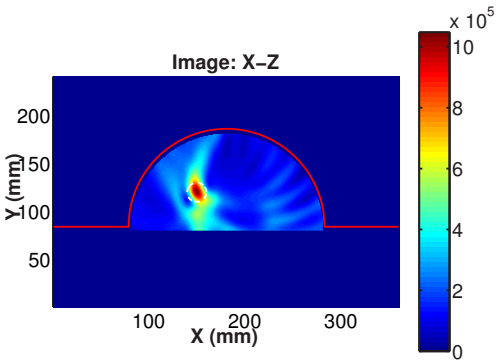

(c): DAS-E2

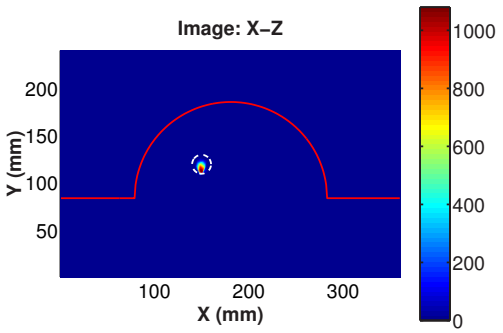

(d): RCB-E2

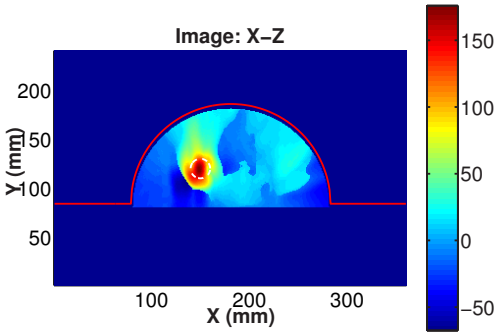

(e): DAS-P

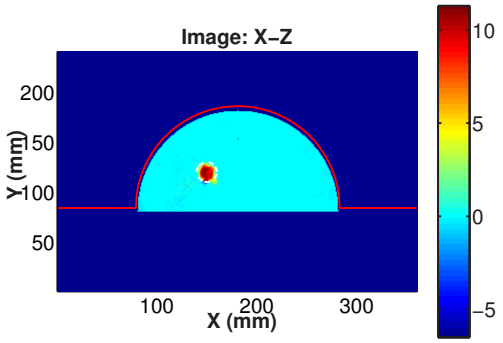

(f): ART-P

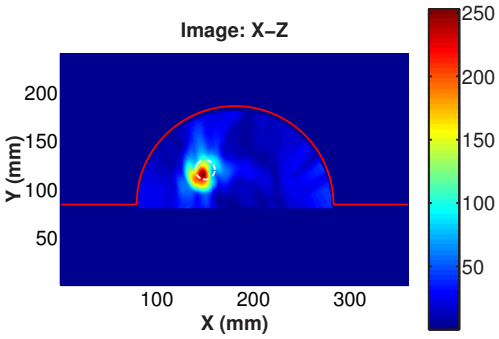

(g): DAS-PP

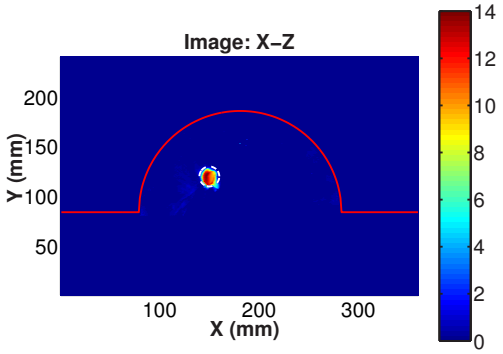

(h): ART-PP

Figure 4–6: Reconstructed images based on the 2-D simulated breast model with one large tumor (1 cm in diameter). The white circle in the image corresponds to the actual shape of the tumor. (a): DAS-C; (b): DAS-E1; (c) DAS-E2; (d): RCB-E2, with $\varepsilon = 0.1M$; (e): DAS-P; (f): ART-P, with $\varepsilon = 0.1M$; (g): DAS-PP; (h): ART-PP, with $\varepsilon = 0.1M$.

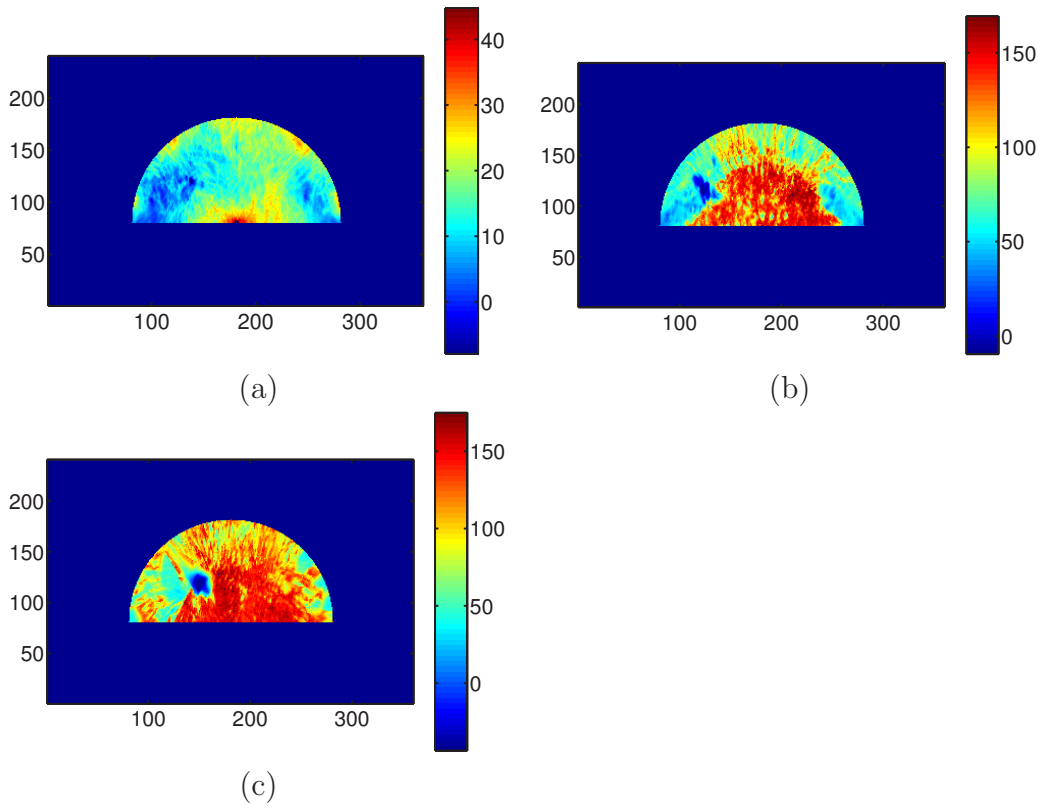

Figure 4–7: The values of μ used in ART, on dB scale, in the cases of: (a): single 2 mm-diameter tumor; (b): two 2 mm spaced 2 mm-diamter tumors; (c): 1 cm-diameter tumor.

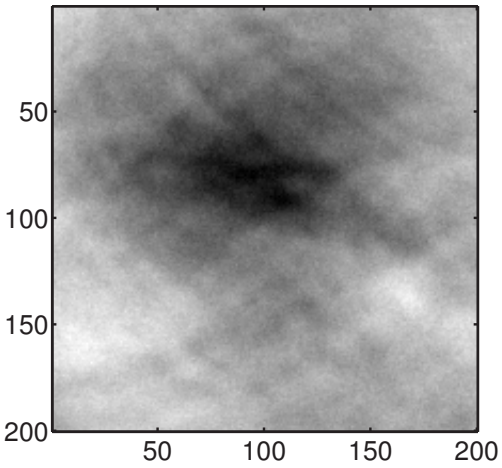

(a): DAS-C

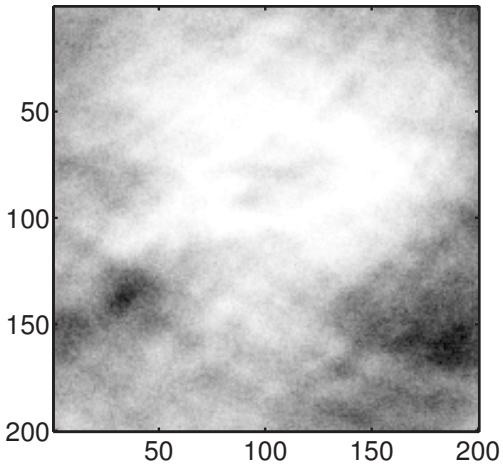

(b): DAS-E1

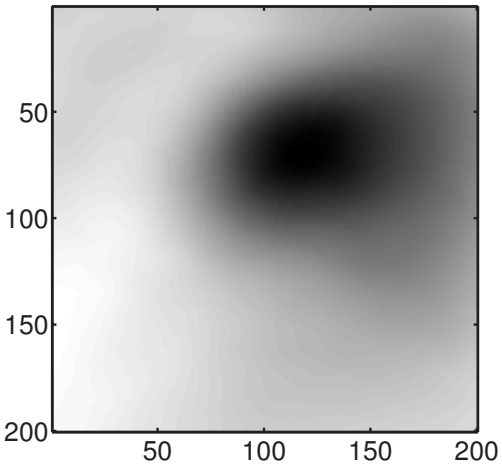

(c): DAS-E2

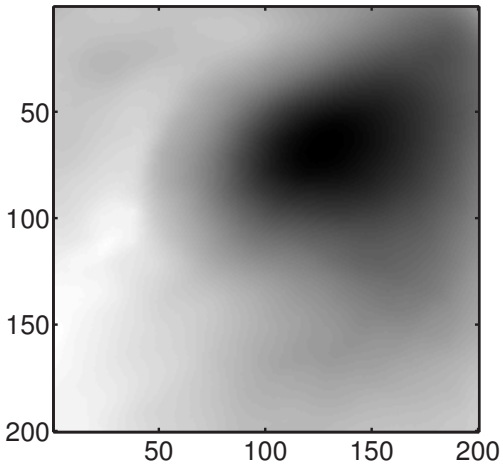

(d): RCB-E2

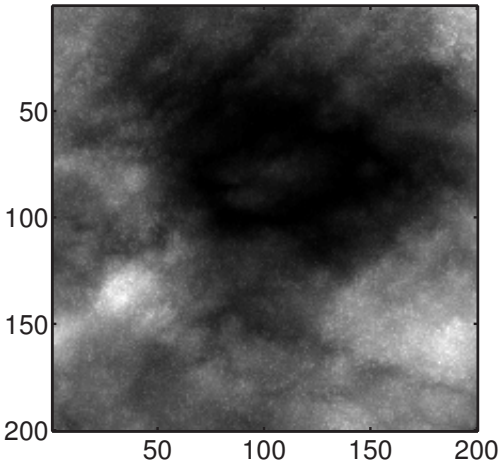

(e): DAS-P

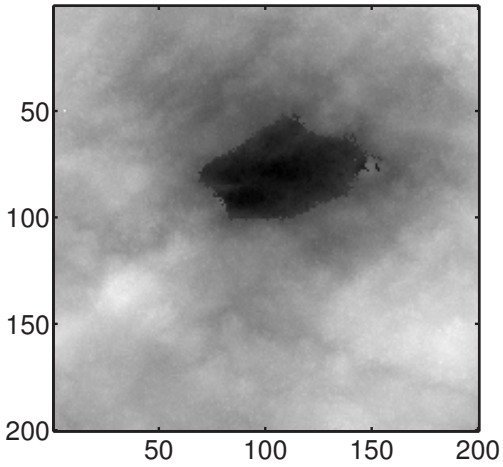

(f): ART-P

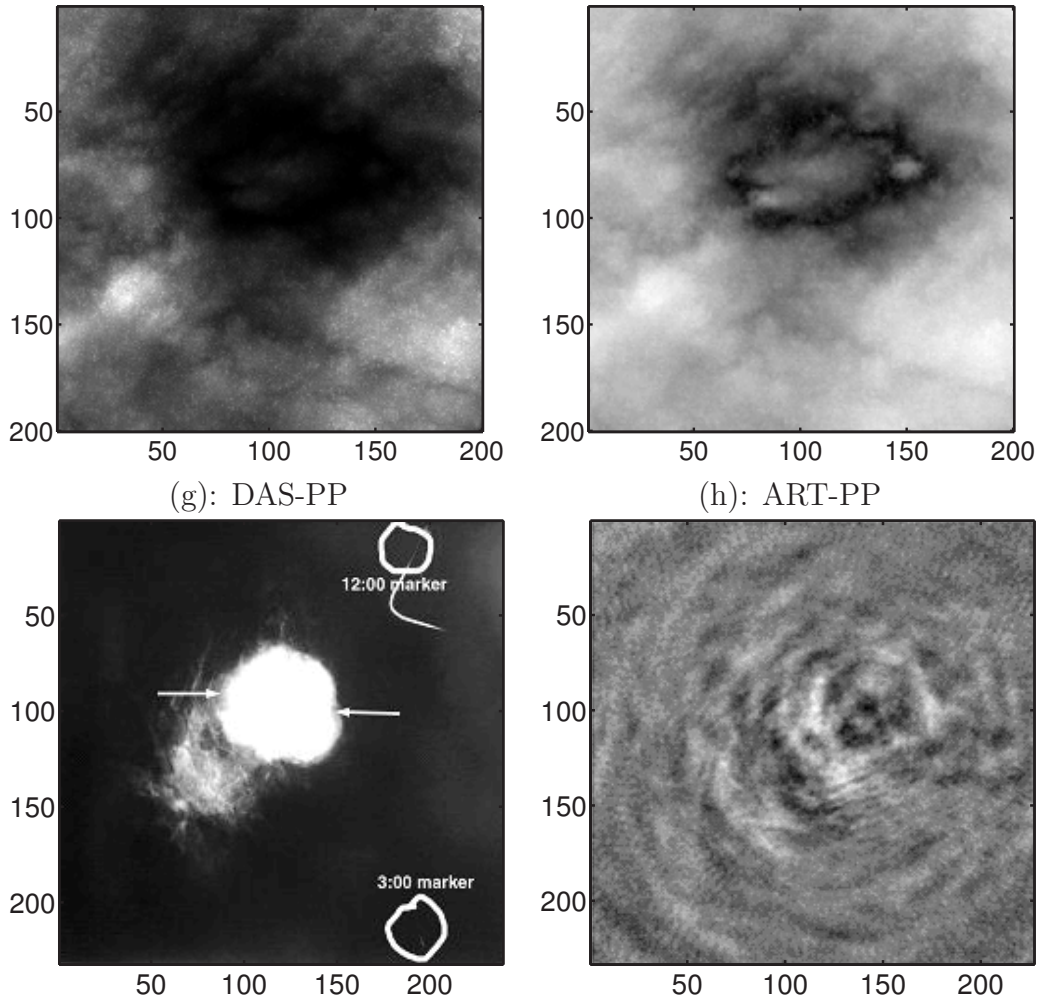

(g): DAS-PP (h): ART-PP

(i): X-ray image (j): Inverse Solution

Figure 4–8: Reconstructed images for breast specimen I. (a): DAS-C; (b): DAS-E1; (c) DAS-E2; (d): RCB-E2, with $\varepsilon = 0.5M$; (e): DAS-P; (f): ART-P, with $\varepsilon = 0.5M$; (g): DAS-PP; (h): ART-PP, with $\varepsilon = 0.5M$; (i): X-ray image; (j): Inverse solution.

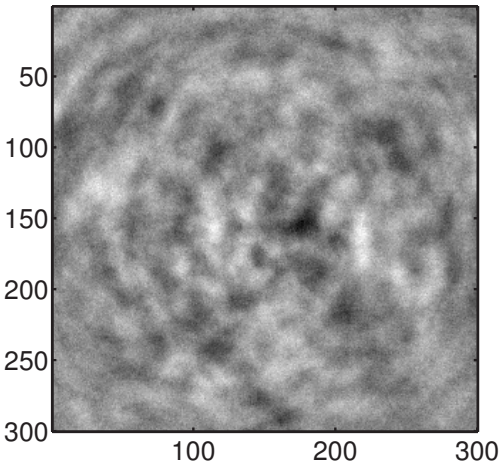

(a): DAS-C

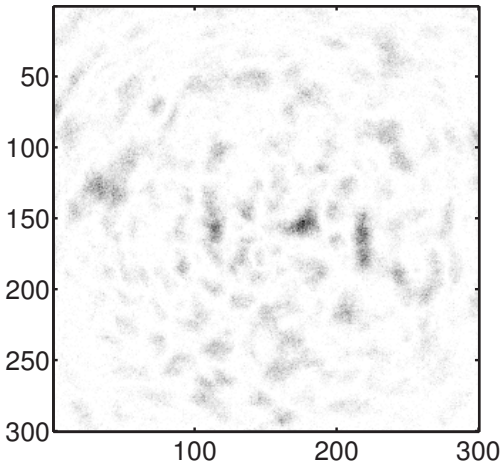

(b): DAS-E1

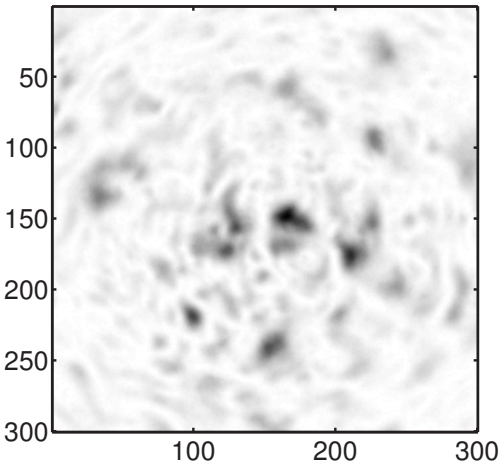

(c): DAS-E2

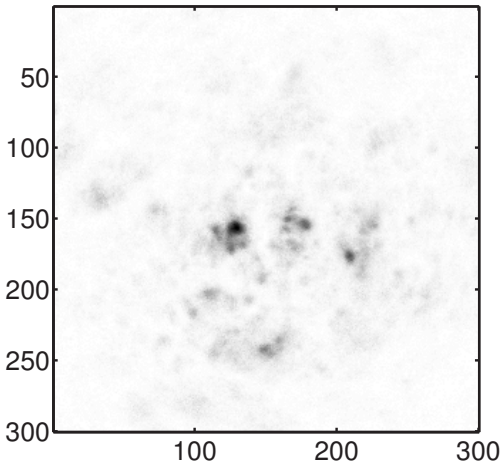

(d): RCB-E2

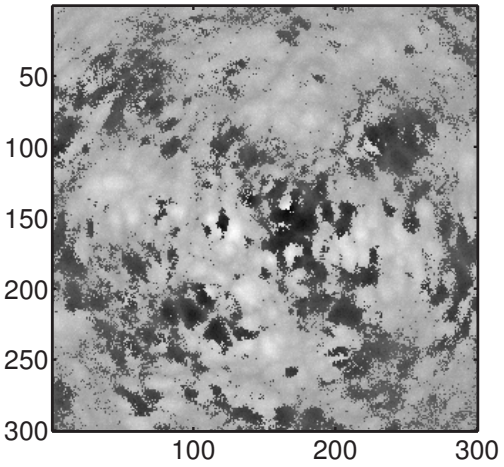

(e): DAS-P

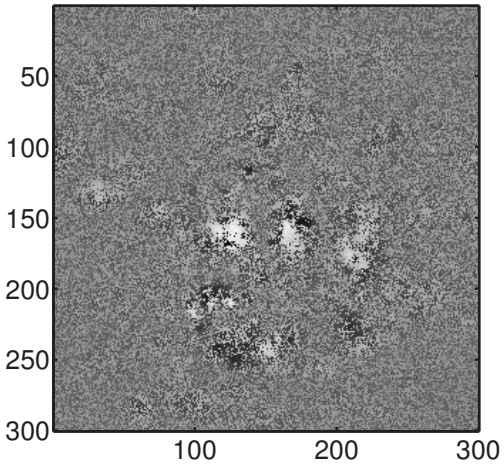

(f): ART-P

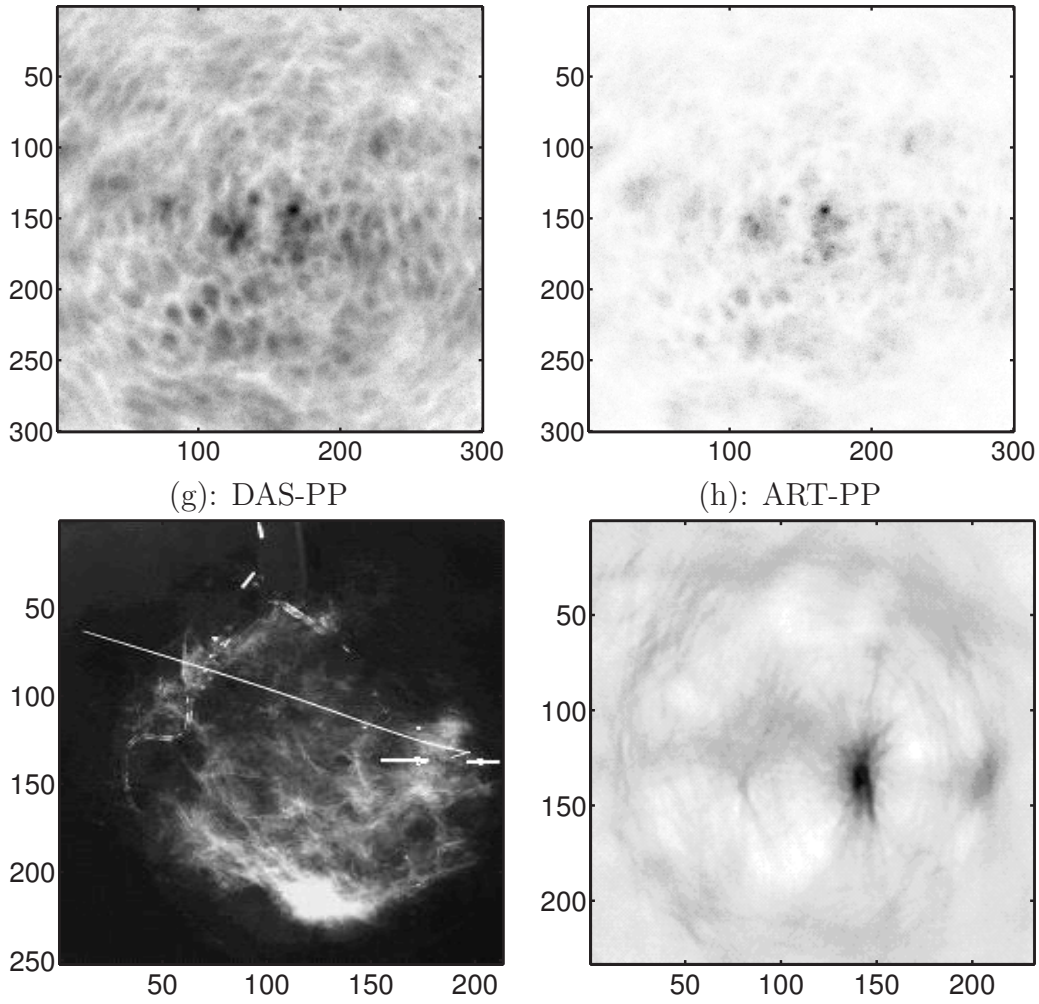

(g): DAS-PP (h): ART-PP

(i): X-ray image (j): Inverse Solution

Figure 4–9: Reconstructed images for breast specimen II. (a): DAS-C; (b): DAS-E1; (c) DAS-E2; (d): RCB-E2, with $\varepsilon = 0.5M$; (e): DAS-P; (f): ART-P, with $\varepsilon = 0.5M$; (g): DAS-PP; (h): ART-PP, with $\varepsilon = 0.5M$; (i): X-ray image; (j): Inverse solution.

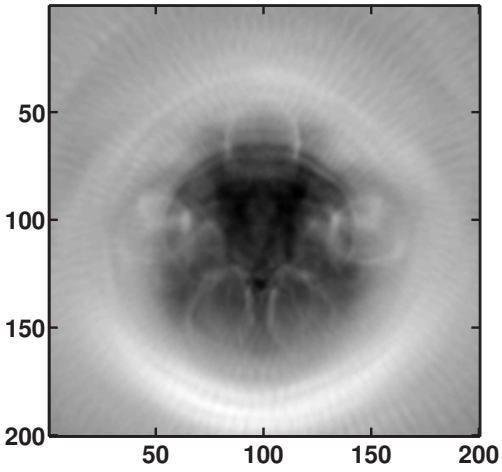

(a): DAS-C

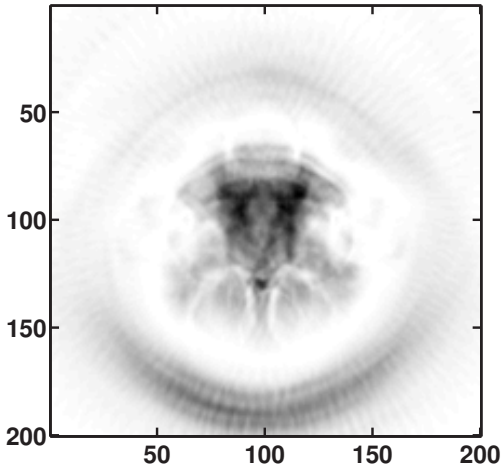

(b): DAS-E1

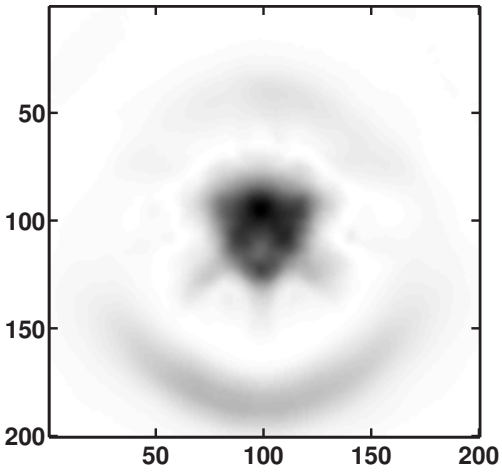

(c): DAS-E2

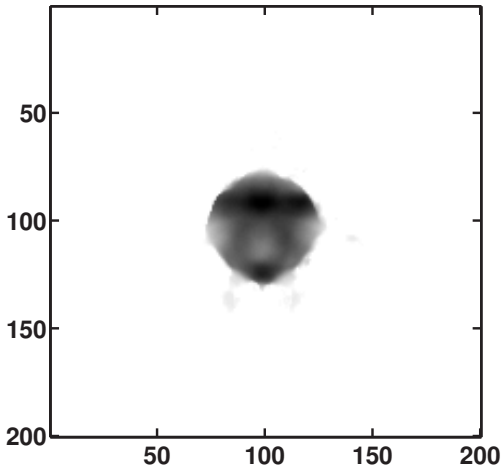

(d): RCB-E2

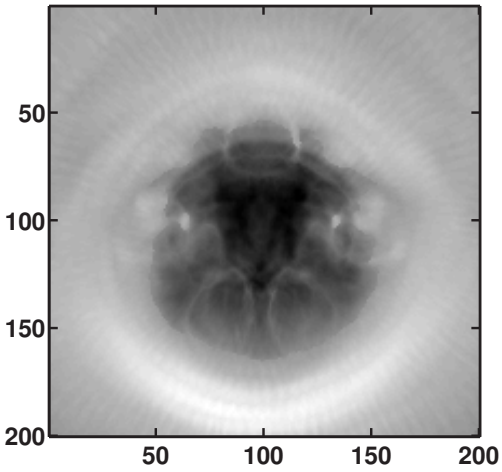

(e): DAS-P

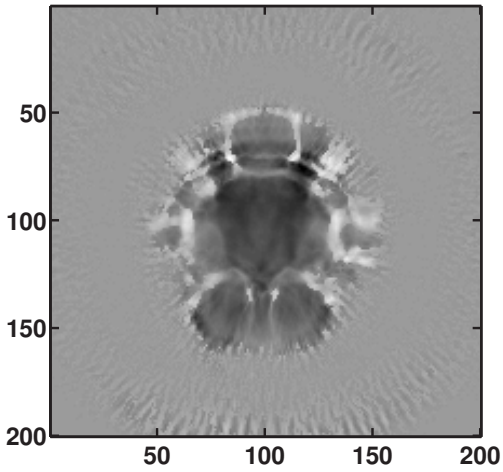

(f): ART-P

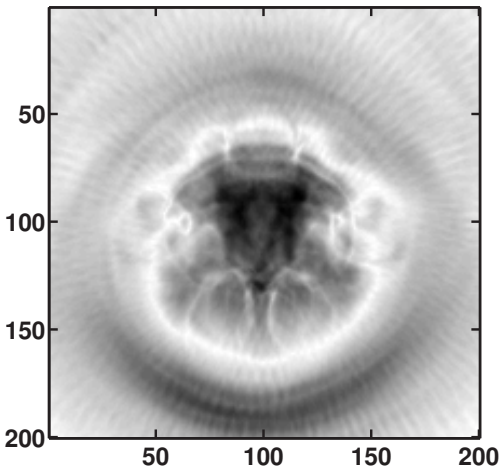

(g): DAS-PP

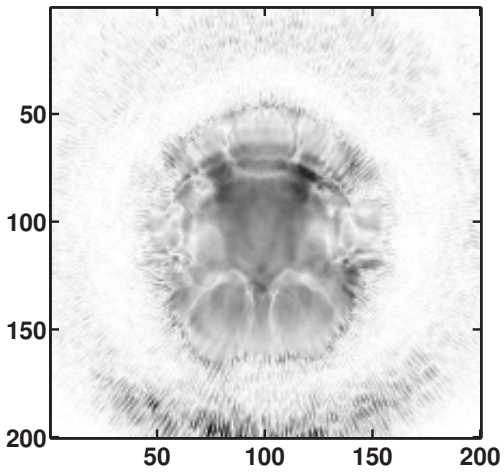

(h): ART-PP

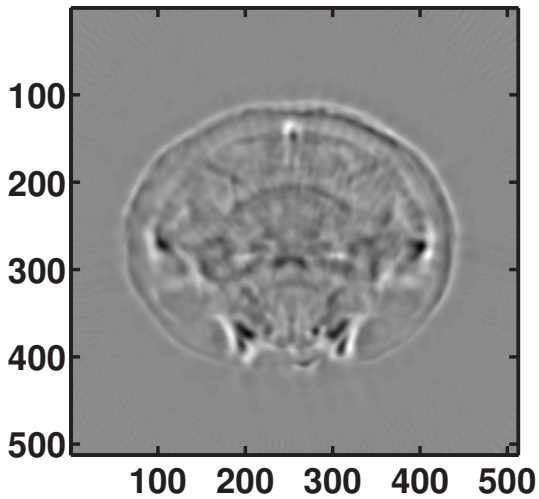

(i): Inverse Solution

Figure 4–10: Reconstructed images for the mouse brain. (a): DAS-C; (b): DAS-E1; (c) DAS-E2; (d): RCB-E2, with $\varepsilon = 0.6M$; (e): DAS-P; (f): ART-P, with $\varepsilon = 0.6M$; (g): DAS-PP; (h): ART-PP, with $\varepsilon = 0.6M$; (i): Inverse solution.

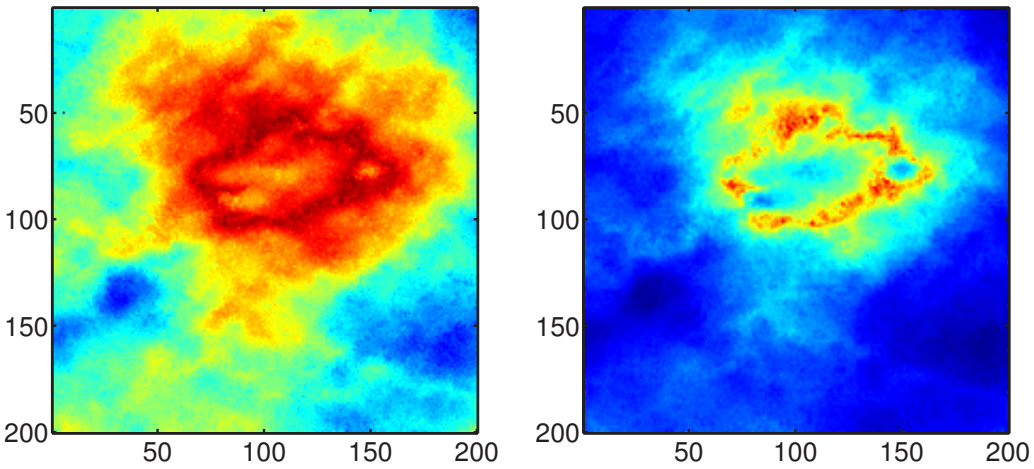

(a) (b)

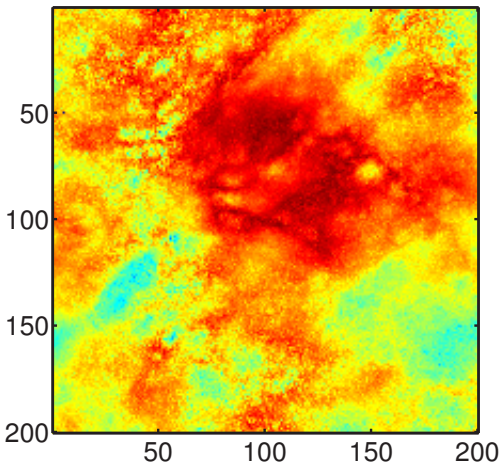

(c)

Figure 4–11: Effects of uncertainty parameter ε on ART-PP, with a searching range [-3,3]. (a): $\varepsilon = 0.7M$; (b): $\varepsilon = 0.5M$; (c): $\varepsilon = 0.3M$.

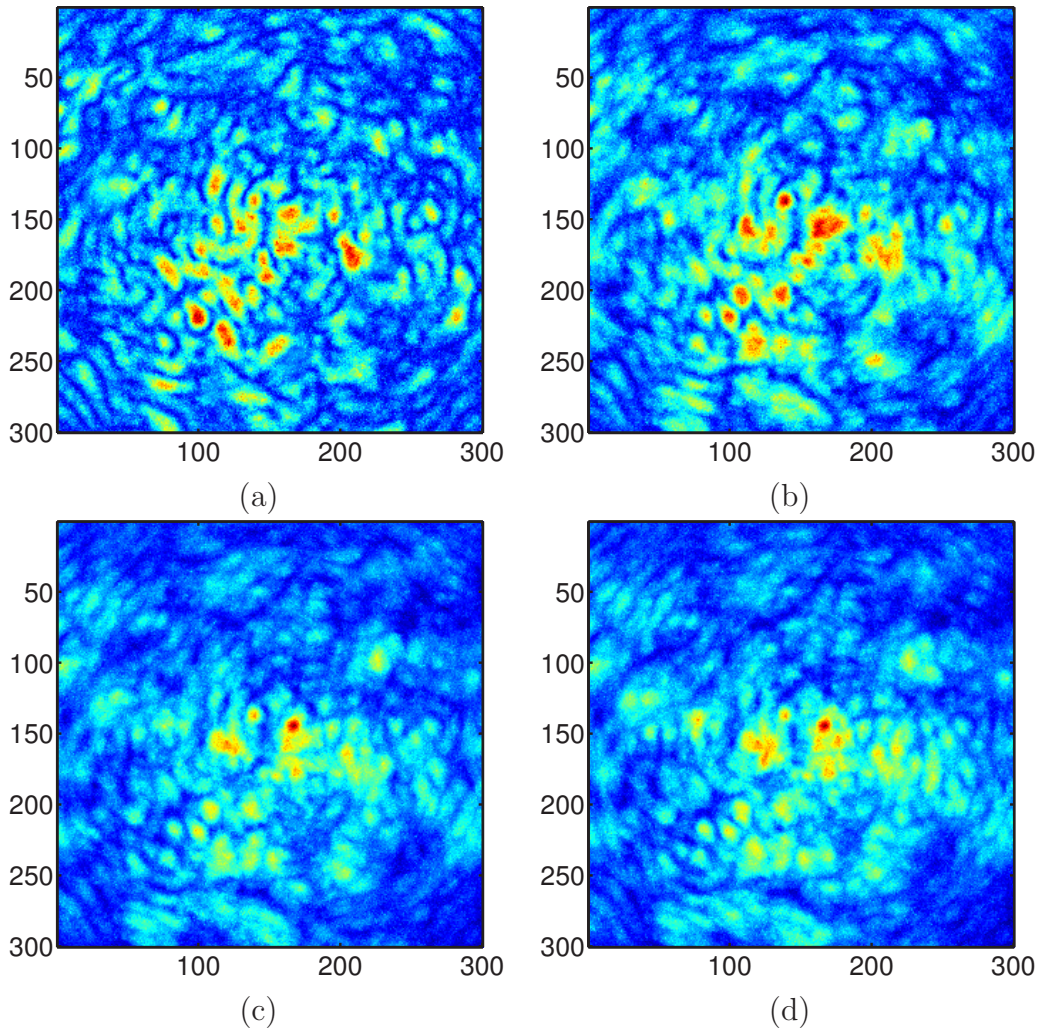

Figure 4–12: Effects of the searching range on the DAS-PP images. (a): searching range [-20, 20]; (b): searching range: [-40, 40]; (c): searching range [-60, 60]; (d): searching range: [-80, 80].

CHAPTER 5
CONCLUSIONS AND FUTURE WORK

In this dissertation, we propose new Adaptive and Robust Techniques (ART) for thermoacoustic tomography, and compare their performances with other existing methods. ART is robust to the amplitude and phase distortions in the recorded signals caused by the acoustic heterogeneity of biological tissues. ART consists of three steps: in the first step, ART uses the data-adaptive Robust Capon Beamforming (RCB) for waveform estimation; in the second step of ART, a simple yet effective peak searching method is used to mitigate the phase distortion in the estimated waveform; in the third step, the response intensity is calculated for the focal point using various approaches, among which the peak-to-peak difference measure further enhances the image contrast. The parameters used in ART: the uncertainty set size and the searching range width, can be determined by using the estimates of arrival time difference variance, and adjusted according to the imaging quality.

Examples based on a numerically simulated 2-D breast model and three sets of experimentally measured data from human mastectomy specimens and a mouse brain demonstrate the excellent performance of ART: high resolution, low-side lobe level, and much improved interference suppression capability. Also, these examples demonstrate that ART is promising in detect tumors in the real breast tissues with accurate location and size, and in brain imaging.

Future work may be to incorporate wideband signal processing techniques in ART, and to use the image registration techniques to align the images formed by different methods.

5.1 Wideband Signal Processing

We could consider using wideband signal model, such as Auto-Regression (AR) model or Auto-Regression Moving Average (ARMA) model [46], to fit the thermoacoustic signals, since they are wideband. The wideband signal processing technique could be employed. For example, in ART signals are processed in time domain based on time delay; we could also consider using tap and delay line [47] rather than a weight vector to estimate the signal waveform. Also, we could consider the frequency domain wideband signal processing approach: divide the wideband signal signal into narrowband frequency bins, and then apply incoherent or coherent narrowband processing [47]. Wideband signal processing has more degree of freedom hence would be more robust to signal waveform distortions, but they require higher computational complexity than the weight vector approach in ART. A good tradeoff could be sought.

5.2 Image Registration

Image registration techniques could be used to align images about one object, obtained from different imaging methods, or even different imaging modalities. In our numerical examples, we found that images about one object could take one quite different appearances. A spatial alignment of the features in different images is often desired. For example, in the experimental example the mouse brain image reconstructed by ART-P, in Figure 4–10(f), shows quite different details to that by the inverse solution, in Figure 4–10(i), but we can observe some correspondence between the two Figures. Image registration aims to find the correspondence, or to spatially align images about one object [48].

The registration algorithms could be based on the segmented features, or the small vortexes (a larger unit than image pixel) [49]. The alignment in image registration could be rigid, which means only linear image transformation is used, or non-rigid, which means that non-lineaer image transformation could also be used. A comprehensive software called MAIMI Fuse [50], developed by Meyer *etal.*, includes

many algorithms, feature based or vortex based, rigid (using linear image transformation) or non-rigid (using non-linear image transformation). In the future, we could consider using image registration to cross-validate the images formed by different methods.

REFERENCES

[1] G. Ku, B. D. Fornage, X. Jin, M. Xu, K. K. Hunt, and L. V. Wang, "Thermoacoustic and photoacoustic tomography of thick biological tissues toward breast imaging," *Technology in Cancer Research & Treatment*, vol. 4, pp. 1–7, Oct. 2005.

[2] G. Ku, X. Wang, G. Stoica, and L. V. Wang, "Multiple-bandwidth photoacoustic tomography," *Physics in Medicine and Biology*, vol. 49, pp. 1329–1338, 2004.

[3] R. A. Kruger, P. Liu, Y. R. Fang, and C. R. Appledorn, "Photoacoustic ultrasound (PAUS) - reconstruction tomography," *Med. Phys.*, vol. 22, pp. 1605–1609, Oct. 1995.

[4] R. A. Kruger, K. K. Kopecky, A. M. Aisen, D. R. Reinecke, G. A. Kruger, and W. L. Kiser, "Thermoacoustic ct with radio waves: a medical imaging paradigm," *Radiology*, vol. 211, pp. 275–278, Apr. 1999.

[5] L. V. Wang, X. Zhao, H. Sun, and G. Ku, "Microwave-induced acoustic imaging of biological tissues," *Med. Phys.*, vol. 70, pp. 3744–3748, Sept. 1999.

[6] R. A. Kruger, K. D. Miller, H. E. Reynolds, W. L. Kiser, D. R. Reinecke, and G. A. Kruger, "Breast cancer in vivo: Contrast enhancement with thermoacoustic CT at 434 MHz - feasibility study," *Radiology*, vol. 216, pp. 279–283, 2000.

[7] S. S. Chaudhary, R. K. Mishra, A. Swarup, and J. M. Thomas, "Dielectric properties of normal and malignant human breast tissues at radiowave and microwave frequencies," *Indian Journal of Biochemistry and Biophysics*, vol. 21, pp. 76–79, February 1984.

[8] W. T. Joines, Y. Zhang, C. Li, and R. L. Jirtel, "The measured electrical properties of normal and malignant human tissues from 50 to 900 Mhz," *Medical Physics*, vol. 21, pp. 547–550, April 1994.

[9] W. Joines, R. Jirtle, M. Rafal, and D. Schaeffer, "Microwave power absorption differences between normal and malignant tissue," *Int. J. Radiat. Oncol., Biol., Phys.*, no. 6, pp. 681–687, 1980.

[10] Y. Xu and L. V. Wang, "Signal processing in scanning thermoacoustic tomography in biological tissues," *Am. Assoc. Phys. Med.*, vol. 28, no. 7, pp. 1519–1524, 2001.

[11] G. Ku and L. V. Wang, "Scanning microwave-induced thermoacoustic tomography: Signal, resolution, and contrast," *Med. Phys.*, vol. 28, pp. 4–10, 2001.

[12] M. H. Xu, G. Ku, and L. V. Wang, "Microwave-induced thermoacoustic tomography using multi-sector scanning," *Med. Phys.*, vol. 28, pp. 1958–1963, 2001.

[13] M. A. Anastasio, J. Zhang, X. Pan, Y. Zou, G. Ku, and L. V. Wang, "Half-time image reconstruction in thermoacoustic tomography," *IEEE Trans. Med. Imag.*, vol. 24, pp. 199–210, Feb. 2005.

[14] Y. Xu, D. Feng, and L. V. Wang, "Exact frequency-domain reconstruction for thermoacoustic tomography: I. Planar geometry," *IEEE Trans. Med. Imag.*, vol. 21, pp. 823–828, 2002.

[15] Y. Xu, M. Xu, and L. V. Wang, "Exact frequency-domain reconstruction for thermoacoustic tomography: II. Cylindrical geometry," *IEEE Trans. Med. Imag.*, vol. 21, pp. 829–833, 2002.

[16] M. Xu and L. V. Wang, "Time-domain reconstruction for thermoacoustic tomography in a spherical geometry," *IEEE Trans. Med. Imag.*, vol. 21, pp. 814–822, Jul. 2002.

[17] M. Xu, Y. Xu, and L. V. Wang, "Time-domain reconstruction algorithms and numerical simulations for thermoacoustic tomography in various geometries," *IEEE Trans. Biomed. Eng.*, vol. 50, pp. 1086–1099, Sep. 2003.

[18] C. G. A. Hoelen and F. F. M. de Mul, "Image reconstruction for photoacoustic scanning of tissue structures," *Applied Optics*, vol. 39, no. 31, pp. 5872–5883, 2000.

[19] D. Feng, Y. Xu, G. Ku, and L. V. Wang, "Microwave-induced thermoacoustic tomography: Reconstruction by synthetic aperture," *Med. Phys.*, vol. 28, pp. 2427–2431, Dec. 2001.

[20] Y. V. Zhulina, "Optimal statistical approach to optoacoustic image reconstruction," *Applied Optics*, vol. 39, no. 32, pp. 5971–5977, 2000.

[21] J. Li, P. Stoica, and Z. Wang, "On robust Capon beamforming and diagonal loading," *IEEE Transactions on Signal Processing*, vol. 51, pp. 1702–1715, July 2003.

[22] P. Stoica, Z. Wang, and J. Li, "Robust Capon beamforming," *IEEE Signal Processing Letters*, vol. 10, pp. 172–175, June 2003.

[23] G. Kossoff, E. K. Fry, and J. Jellins, "Average velocity of ultrasound in the human female breast," *J. Acoust. Soc. Am.*, vol. 53, no. 6, pp. 1730–1736, 1973.

[24] T. Szabo, *Diagnostic Ultrasound Imaging: Inside Out.* Academic Press, Sept. 2004.

[25] Y. Xu and L. V. Wang, "Effects of acoustic heterogeneity in breast thermoacoustic tomography," *IEEE. Trans. Ultrason., Ferroelect. Freq. Contr.*, vol. 50, pp. 1134–1146, Sep. 2003.

[26] Y. Sumino and R. Waag, "Measurements of ultrasonic pulse arrival time differences produced by abdominal wall specimens," *J. Acoust. Soc. Am.*, vol. 90, pp. 2924–2930, Dec. 1991.

[27] Q. Zhu and B. D. Steinberg, "Wavefront amplitude distribution in the female breast," *J. Acoust. Soc. Am.*, vol. 96, pp. 1–9, Jul. 1994.

[28] L. M. Hinkelman and D. Liu, "Measurement and correction of ultrasonic pulse distortion produced by human breast," *J. Acoust. Soc. Am.*, vol. 97, pp. 1958–1969, Mar. 1995.

[29] L. Nock and G. Trahey, "Phase aberration correction in medical ultrasound using speckle brightness as a quality factor," *J. Acoust. Soc. Am.*, vol. 85, pp. 1819–1833, May 1985.

[30] D. Liu and R. C. Waag, "Time-shift compensation of ultrasonic pulse focus degradation using least-mean-square error estimates of arrival time," *J. Acoust. Soc. Am.*, vol. 95, pp. 542–555, Jan. 1994.

[31] D. Liu and R. Waag, "Correction of ultrasonic wavefront distortion using backpropagation and a reference waveform method for time-shift compensation," *J. Acoust. Soc. Am.*, vol. 96, pp. 649–660, Aug. 1994.

[32] Q. Zhu and B. D. Steinberg, "Deaberration of incoherent wavefront distortion: An approach toward inverse filtering," *IEEE Trans. Ultrason., Ferroelect, Freq. Contr.*, vol. 44, pp. 575–589, 1997.

[33] W. F. Walker and G. E. Trahey, "A fundamental limit on delay estimation using partially correlated speckle signals," *IEEE Trans. Ultrason., Ferroelect, Freq. Contr.*, vol. 42, pp. 301–308, Mar. 1995.

[34] M. Xu and L. V. Wang, "Pulsed-microwave-induced thermoacoustic tomography: Filtered backprojection in a circular measurement configuration," *Med. Phys.*, vol. 29, no. 8, pp. 1661–1669, 2002.

[35] J. Li and P. Stoica, eds., *Robust Adaptive Beamforming.* New York, NY: John Wiley & Sons, 2005.

[36] J. Capon, "High resolution frequency-wavenumber spectrum analysis," *Proceedings of the IEEE*, vol. 57, pp. 1408–1418, August 1969.

[37] S. A. Vorobyov, A. B. Gershman, and Z. Luo, "Robust adaptive beamforming using worst-case performance optimization: a solution to the signal mismatch problem," *IEEE Transactions on Signal Processing*, vol. 51, pp. 313–324, February 2003.

[38] X. Li and S. C. Hagness, "A confocal microwave imaging algorithm for breast cancer detection," *IEEE Microwave and Wireless Components Letters*, vol. 11, pp. 130–132, March 2001.

[39] R. Nilavalan, A. Gbedemah, I. J. Craddock, X. Li, and S. C. Hagness, "Numerical investigation of breast tumour detection using multi-static radar," *IEE Electronics Letters*, vol. 39, December 2003.

[40] Y. Xie, B. Guo, J. Li, and P. Stoica, "Novel multistatic adaptive microwave imaging methods for early breast cancer detection," *EURASIP Journal on Applied Signal Processing*, vol. 2006, pp. 1–12, 2006.

[41] B. Guo, Y. Wang, J. Li, P. Stoica, and R. Wu, "Microwave imaging via adaptive beamforming methods for breast cancer detection,," *Journal of Electromagnetic Waves and Applications*, vol. 20, no. 1, pp. 53–63, 2006.

[42] A. Taflove and S. C. Hagness, *Computational Electrodynamics: The Finite-Difference Time-Domain Method*. Boston, MA: Artech House, third ed., July 2005.

[43] A. J. Surowiec, S. S. Stuchly, J. R. Barr, and A. Swarup, "Dielectric properties of breast carcinoma and the surrounding tissues," *IEEE Transactions of Biomedical Engineering*, vol. 35, pp. 257–263, April 1988.

[44] A. Swarup, S. S. Stuchly, and A. J. Surowiec, "Dielectric properties of mouse MCA1 fibrosarcoma at different stages of development," *Bioelectromagnetics*, vol. 12, no. 1, pp. 1–8, 1991.

[45] C. Gabriel, R. W. Lau, and S. Gabriel, "The dielectric properties of biological tissues: II. measured in the frequency range 10Hz to 20GHz," *Physics in Medicine and Biology*, vol. 41, pp. 2251–2269, November 1996.

[46] P. Stoica and R. Moses, *Spectral Analysis of Signals*. Upper Saddle River, NJ: Prentice Hall, 2005.

[47] H. L. V. Trees, *Optimum Array Processing*. New York, NY: John Wiley & Sons, March 2002.

[48] J. B. A. Maintz and M. A. Viergever, "A survey of medical image registration," *Medical Image Analysis*, vol. 2, pp. 1–36, March 1998.

[49] J. F. Krücker, G. L. LeCarpentier, J. B. Fowlkes, and P. L. Carson, "Rapid elastic image registration for 3-D ultrasound," *IEEE Transactions on Medical Imaging*, vol. 21, pp. 1384–1394, November 2002.

[50] C. R. Meyer, J. L. Boes, B. Kim, P. H. Bland, G. L. LeCarpentier, J. B. Fowlkes, M. A. Roubidoux, and P. L. Carson, "Semiautomatic registration of volumetric ultrasound scans," *Ultrasound Medical Biology*, vol. 25, pp. 339–347, 1999.

BIOGRAPHICAL SKETCH

Yao Xie was born in Huhhot, Inner Mongolia, People's Republic of China, in 1982. She received the B.Sc. degree in *Electrical Engineering and Information Science* from the *University of Science and Technology of China (USTC)*, Hefei, China, in July, 2004, and M.Sc. degree in the Department of *Electrical and Computer Engineering* at *University of Florida*, Gainesville, Florida, in August, 2006. She is a member of Tau Beta Pi and Etta Kappa Nu. She was the first place winner in the Student Best Paper Contest at the 2005 Annual Asilomar Conference on Signals, Systems, and Computers, for her work on breast cancer detection.

I certify that I have read this study and that in my opinion it conforms to acceptable standards of scholarly presentation and is fully adequate, in scope and quality, as a dissertation for the degree of Master of Science.

Jian Li, Chair,
Professor of
Electrical and Computer Engineering

I certify that I have read this study and that in my opinion it conforms to acceptable standards of scholarly presentation and is fully adequate, in scope and quality, as a dissertation for the degree of Master of Science.

Liuqing Yang
Assistant professor of
Electrical and Computer Engineering

I certify that I have read this study and that in my opinion it conforms to acceptable standards of scholarly presentation and is fully adequate, in scope and quality, as a dissertation for the degree of Master of Science.

Kenneth Clint Slatton
Assistant Professor of
Electrical and Computer Engineering,
and Civil and Coastal Engineering

This dissertation was submitted to the Graduate Faculty of the College of Engineering and to the Graduate School and was accepted as partial fulfillment of the requirements for the degree of Master of Science.

August 2006

Pramod P. Khargonekar
Dean, College of Engineering

Kenneth Gerhardt
Dean, Graduate School

GROWTH CURVE MODELS IN SIGNAL PROCESSING APPLICATIONS

Yao Xie
(352) 871–0826
Department of Electrical and Computer Engineering
Chair: Jian Li
Degree: Master of Science
Graduation Date: August 2006

Thermoacoustic tomography (TAT) is an emerging medical imaging technique that has excellent imaging quality: high contrast, in differentiating various tissues, and high resolution, in rendering details in the image. TAT can be potentially used in a wide span of medical imaging applications, including early breast cancer detection. Breast cancer takes tremendous toll to our society. Diagnosis at the earliest stage is the best hope of surviving breast cancer.

One of the key problems encountered in TAT is the image reconstruction from TAT signals. The current image reconstruction methods used in TAT, such as the widely used Delay-and-Sum (DAS) approaches, are data-independent and suffer from poor imaging quality: low resolution, high sidelobe levels, and inadequate interference rejection capabilities. Also, The image quality degradation problem due to the distortions of TAT signals while propagating in the biological tissues has not been properly handled in the existing methods.

In this thesis, we present Adaptive and Robust Techniques (ART) for TAT, with applications in breast cancer detection and mouse brain imaging. The data-adaptive ART can have much better imaging quality: better resolution, interference rejection capabilities, than their data-independent counterparts. By allowing certain uncertainties, ART can be used to mitigate the amplitude and phase distortion problems encountered in TAT. Using both simulated and experimentally measured data, we demonstrate the excellent performance of ART: high resolution, low sidelobe level, and much better interference rejection capability.